



OPEN ACCESS

EDITED BY

Eli Fernandez-de Gortari,
International Iberian Nanotechnology
Laboratory (INL), Portugal

REVIEWED BY

Abraham Madariaga mazon,
National Autonomous University of
Mexico, Mexico
Antonio Romo-Mancillas,
Universidad Autónoma de Querétaro,
Mexico
Luis Olivares Quiroz,
Universidad Autónoma de la Ciudad de
México, Mexico
Lu Shaoyong,
Shanghai Jiao Tong University, China

*CORRESPONDENCE

Enrique García-Hernández,
egarciah@unam.mx

[†]These authors have contributed equally
to this work

SPECIALTY SECTION

This article was submitted to
Experimental Pharmacology and Drug
Discovery,
a section of the journal
Frontiers in Pharmacology

RECEIVED 04 August 2022

ACCEPTED 03 October 2022

PUBLISHED 14 October 2022

CITATION

Cofas-Vargas LF, Mendoza-Espinosa P,
Avila-Barrientos LP, Prada-Gracia D,
Riveros-Rosas H and
García-Hernández E (2022), Exploring
the druggability of the binding site of
aurovertin, an exogenous allosteric
inhibitor of F₀F₁-ATP synthase.
Front. Pharmacol. 13:1012008.
doi: 10.3389/fphar.2022.1012008

COPYRIGHT

© 2022 Cofas-Vargas, Mendoza-
Espinosa, Avila-Barrientos, Prada-
Gracia, Riveros-Rosas and García-
Hernández. This is an open-access
article distributed under the terms of the
[Creative Commons Attribution License
\(CC BY\)](https://creativecommons.org/licenses/by/4.0/). The use, distribution or
reproduction in other forums is
permitted, provided the original
author(s) and the copyright owner(s) are
credited and that the original
publication in this journal is cited, in
accordance with accepted academic
practice. No use, distribution or
reproduction is permitted which does
not comply with these terms.

Exploring the druggability of the binding site of aurovertin, an exogenous allosteric inhibitor of F₀F₁-ATP synthase

Luis Fernando Cofas-Vargas^{1†}, Paola Mendoza-Espinosa^{1,2†},
Luis Pablo Avila-Barrientos¹, Diego Prada-Gracia³,
Héctor Riveros-Rosas⁴ and Enrique García-Hernández^{1*}

¹Universidad Nacional Autónoma de México, Instituto de Química, Ciudad Universitaria, Mexico City, Mexico, ²Tecnológico de Monterrey, The Institute for Obesity Research, Monterrey, Mexico, ³Unidad de Investigación en Biología Computacional y Diseño de Fármacos, Hospital Infantil de México Federico Gómez, Mexico City, Mexico, ⁴Departamento de Bioquímica, Facultad de Medicina, Universidad Nacional Autónoma de México, Avenida Universidad 3000, Cd. Universitaria, Mexico City, Mexico

In addition to playing a central role in the mitochondria as the main producer of ATP, F₀F₁-ATP synthase performs diverse key regulatory functions in the cell membrane. Its malfunction has been linked to a growing number of human diseases, including hypertension, atherosclerosis, cancer, and some neurodegenerative, autoimmune, and aging diseases. Furthermore, inhibition of this enzyme jeopardizes the survival of several bacterial pathogens of public health concern. Therefore, F₀F₁-ATP synthase has emerged as a novel drug target both to treat human diseases and to combat antibiotic resistance. In this work, we carried out a computational characterization of the binding sites of the fungal antibiotic aurovertin in the bovine F₁ subcomplex, which shares a large identity with the human enzyme. Molecular dynamics simulations showed that although the binding sites can be described as preformed, the inhibitor hinders inter-subunit communications and exerts long-range effects on the dynamics of the catalytic site residues. End-point binding free energy calculations revealed hot spot residues for aurovertin recognition. These residues were also relevant to stabilize solvent sites determined from mixed-solvent molecular dynamics, which mimic the interaction between aurovertin and the enzyme, and could be used as pharmacophore constraints in virtual screening campaigns. To explore the possibility of finding species-specific inhibitors targeting the aurovertin binding site, we performed free energy calculations for two bacterial enzymes with experimentally solved 3D structures. Finally, an analysis of bacterial sequences was carried out to determine conservation of the aurovertin binding site. Taken together, our results constitute a first step in paving the way for structure-based development of new allosteric drugs targeting F₀F₁-ATP synthase sites of exogenous inhibitors.

KEYWORDS

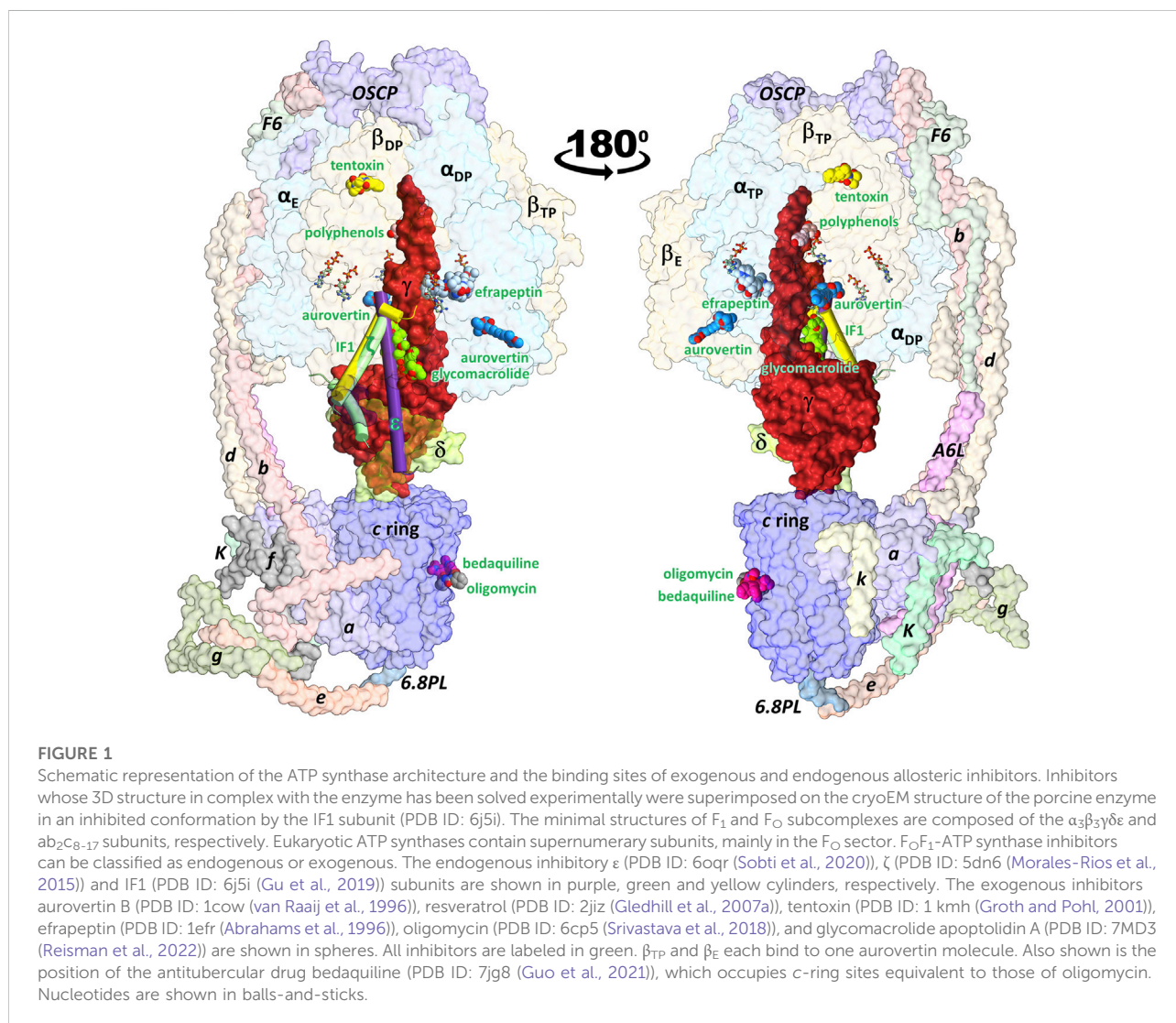
FOF1-ATP synthase inhibition, conformational dynamics, solvent sites, binding free energy, hot spot binding residues, bacterial pathogens

1 Introduction

Because of its crucial role in the production of ATP and its involvement in regulating multiple physiological processes in plasma membranes, an improper function of F_0F_1 -ATP synthase may trigger various diseases in humans, including Alzheimer, Parkinson, amyotrophic lateral sclerosis, diabetes, hypertension, and cancer (Nesci et al., 2019; Galber et al., 2021). There is evidence that F_0F_1 -ATP synthase inhibition results in arrest of both tumor angiogenesis and metastasis (Taurino and Gnoni, 2018). In addition, this enzyme is an attractive new drug target for combating the growing problem of antimicrobial resistance by undermining bacterial bioenergetics (Cook et al., 2014; Hards and Cook, 2018; Ruiz-Blanco et al., 2021; Avila-Barrientos et al., 2022). A salient achievement of the latter has been the design of bedaquiline, a drug used to treat tuberculosis (Lakshmanan and Xavier, 2013; Luo et al., 2020), which spawned the idea of using F_0F_1 -ATP synthase as a

species-specific antimicrobial target. Moreover, there is strong evidence that the inhibition of this enzyme can effectively assist in the interruption of the life cycle of facultative anaerobes with multiresistance, as has been shown for several species of the genera *Streptococcus*, *Staphylococcus*, *Escherichia*, and *Klebsiella* (Bosch et al., 2020; Vestergaard et al., 2021).

All F_0F_1 -ATP synthases share a basic architecture composed of a transmembrane F_0 subcomplex and a solvent-exposed F_1 subcomplex (Figure 1) (Hong and Pedersen, 2003; Kühlbrandt, 2019). F_0 drives rotary motion of the rod-shaped γ subunit using the electrochemical gradient established by the respiratory chain. F_1 carries the catalytic machinery comprising a hexamer of alternating pairs of α/β subunits in which the γ subunit is embedded. The ϵ subunit (δ in mitochondrial ATP synthases) is bound to a solvent-exposed region of the γ subunit. Each of the homologous three-domain α and β subunits contains a nucleotide binding site, but only the β subunits, with the



participation of a few key residues of a neighboring α subunit, are catalytic (Pulido et al., 2010; Salcedo et al., 2014). Following the nucleotide occupancy observed in the first crystal F_1 structure of *Bos taurus* (BtF₁) (Abrahams et al., 1994), the β subunits are commonly referred to as β_E (empty catalytic site), β_{DP} (ADP bound), and β_{TP} (ATP bound), although other nucleotide occupancies and conformations have been seen in later structures (Kühlbrandt, 2019). β_E shows an open conformation, with the C-terminal domain (CTD) largely exposed to the solvent. β_{DP} and β_{TP} adopt closed conformations that largely overlap each other, although β_{DP} packs more extensively against its adjacent subunits. These conformations, in which each β subunit makes unique contacts with the central asymmetric γ subunit, constitute the structural basis of the binding change mechanisms that involves the alternate conformational changes of the β subunits coupled to rotation of the γ subunit (Abrahams et al., 1994).

Modern medicine requires the identification and validation of novel key therapeutic targets to tackle diseases lacking an effective cure, or whose treatment causes significant side effects. The vast majority of drugs approved for clinical use (~99.5%) bind directly to active sites (Sheik Amamuddy et al., 2020). Side effects associated with these orthosteric binders are often related to cross-reactivity with off-target proteins. Instead, allosteric molecules bind to pockets that are less conserved than active sites (Lu et al., 2019; Bhat et al., 2020; Chatzigoulas and Cournia, 2021), providing the opportunity to more selectively modulate targets of interest (Nesci et al., 2019; Chatzigoulas and Cournia, 2021). In particular, allosteric sites that lack endogenous binders (i.e., non-functional allosteric sites) are attractive, as binders designed against them typically require lower potency optimization than drugs raised against orthosteric or allosteric functional sites (Nussinov and Tsai, 2012; Chatzigoulas and Cournia, 2021). In this context, it is relevant that biological evolution has “discovered” hundreds of exogenous molecules that bind to non-functional allosteric sites of F_0F_1 -ATP synthase, blocking the progression of conformational changes that drive the enzyme’s rotary mechanism. This aspect could be particularly useful for the design of specific F_0F_1 -ATP synthase inhibitors, since some regions of the active site of this enzyme are highly conserved in P-loop NTPases (Walker et al., 1982; Leipe et al., 2003).

As illustrated in Figure 1, the binding sites of several allosteric inhibitors have been structurally determined throughout the enzyme (Hong and Pedersen, 2008; Patel et al., 2020). To prevent wasteful consumption of ATP, the ϵ subunit in bacteria and chloroplast, and the supernumerary subunits IF1 and ζ in eukaryotes and α -proteobacteria, respectively, embed a helical domain into a transient cavity formed between α , β and γ subunits, suppressing enzyme rotation (Cingolani and Duncan, 2011; Varghese et al., 2018; Jarman et al., 2021). Similarly, the glycomacrolides apoptolidin A and ammocidin A bind to the same pocket as the endogenous inhibitory subunits (Reisman et al., 2022). Interestingly, these two exogenous binders with unknown biological function

demonstrated efficacy in suppressing leukemia progression. Bacteria and fungi have developed numerous molecules to inhibit the F_0F_1 -ATP synthases of other organisms as a means of self-defense, invasion, or to eliminate competition from other species. The herbicide tentoxin and the antibiotics efrapeptins and aurovertins bind to nonoverlapping pockets at α/β interfaces (Abrahams et al., 1996; van Raaij et al., 1996; Groth and Pohl, 2001). The antibiotic oligomycin binds to an equivalent site of bedaquiline on the c subunits in F_0 (Symersky et al., 2012). Plant polyphenols such as resveratrol, piceatannol, and quercetin bind to a transient cavity formed between α , β and γ subunits, although the functional relevance of their inhibitory effect remains unclear (Gledhill et al., 2007a).

The intersubunit communication events that occur along the rotary mechanism of ATP synthase involve the formation and rupture of multiple pockets. As described above, nature has exploited these transient pockets as sites for allosteric inhibition, in which peptides and small molecules insert like wedges into a gear, preventing progression of the rotary cycle. Therefore, it could be hypothesized they are exploitable pockets to develop potential pharmacological allosteric modulators of this enzyme (Huang et al., 2008; Patel et al., 2020). However, there are no systematic studies aimed at exploring the druggability potential of F_0F_1 -ATP synthase pockets to which exogenous molecules bind. As a first step to pave the way for structure-based development of new allosteric drugs targeting F_0F_1 -ATP synthase, in this work we carried out a computational characterization of the binding sites of the fungal antibiotic aurovertin (AUR). The ability of AUR to inhibit the development of malignant cell lines or tumors through specific binding to F_0F_1 -ATP synthase makes it an attractive model compound to treat different cancer types (Wu et al., 2020). Although not yet experimentally explored, AUR could also cause effects comparable to those elicited by other F_0F_1 -ATP synthase inhibitors in other diseases (Wang et al., 2021), including treatment against bacterial pathogens (Mahajan, 2013). AURs are a group of fungal reduced polyketides with antitumor, nematocidal, and antimicrobial activities that contain a 2,6-dioxabicyclo [3.2.1]octane core attached to a methylated α -pyrone through a triene linker (Patel et al., 2020; Wu et al., 2020; Flores Francisco et al., 2021). There are 21 known AURs (termed A to U). The differences between them are found mainly in the bicyclo moiety, where up to four substitutions can occur, mainly by hydrophobic groups. These molecules are mixed inhibitors. They completely stop ATP synthesis and leave a significant residual activity (up to 40%) in the direction of hydrolysis. The basis for this differential effect on both catalytic activities remains unclear (van Raaij et al., 1996; Johnson et al., 2009).

The crystal structure of the BtF₁ in complex with aurovertin B (AUR B) shows two inhibitor binding sites, one in β_E and one in β_{TP} , in a hydrophobic cleft between the nucleotide binding

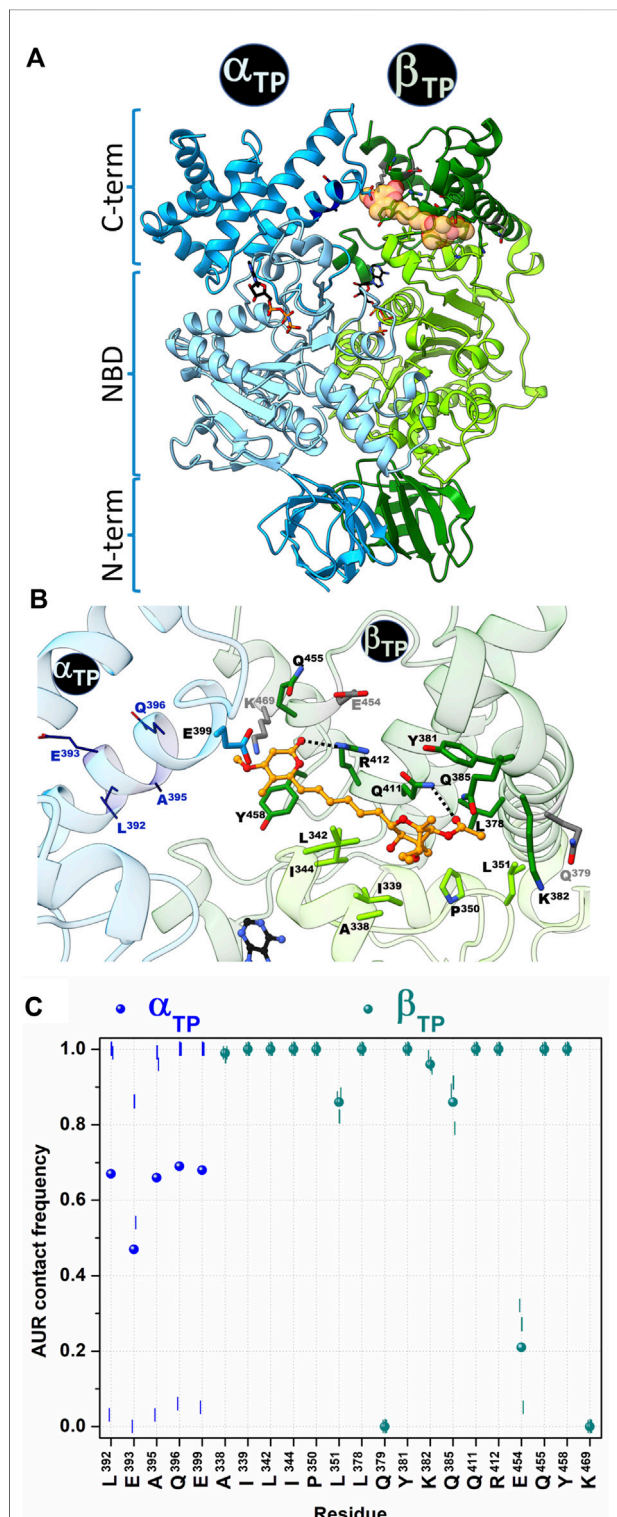


FIGURE 2

Contact analysis at the AUR binding site in β_{TP} . In the crystal structure of BtF₁ complexed with AUR B (PDB ID: 1cow), one inhibitor molecule is bound to β_{TP} and a second to β_E . Only the β_{TP} site is shown. **(A)** Both α and β subunits have a three-domain organization: a β -barrel N-terminal domain (NTD), a central nucleotide binding domain (NBD) and a C-terminal helical domain (Continued)

FIGURE 2 (Continued)

(CTD). The aurovertin binding sites are in equivalent positions in β_E and β_{TP} , in a cavity between NBD and CTD. AUR and nucleotides are shown in yellow spheres and sticks, respectively. **(B)** Structure of the AUR binding site. Residues in the crystal structure within 5 Å of the inhibitor are shown in sticks. Three β -subunit residues that lost contact with AUR during MD simulations are in gray. Four α -subunit residues (shown in wireframe) that were initially >5 Å from the inhibitor came into close contact with it during the simulations. AUR is shown in balls-and-sticks. The hydrogen bonds between βR^{412} -O19 and βQ^{411} -O25, which remained formed throughout the simulations, are shown with black dotted lines **(C)** AUR-protein interaction cumulative frequency observed in the MD simulations. The results of the individual trajectories are shown as vertical lines; the circle symbols correspond to the mean values of the three replicas.

domain (NBD) and CTD (Figure 1 and Figure 2A). The closest distance between AUR B and ATP in β_{TP} is ~12 Å, which is consistent with the observed uncompetitive inhibition (van Raaij et al., 1996). Because of a tighter packing, no space for the inhibitor is available in β_{DP} . Thus, the inhibition mechanism has been proposed to consist in sterically preventing the conversion of β_{TP} to β_{DP} (hydrolysis direction) or β_E to β_{DP} (synthesis direction) (van Raaij et al., 1996). AUR B shows the same binding mode at the β_{TP} and β_E sites (β_{TP} -AUR⁺ and β_E -AUR⁺, respectively) interacting with an identical set of 17 β -subunit residues within 5 Å of the inhibitor (Figure 2B). Each site is composed of 1) six hydrophobic NBD residues (βA^{338} , βI^{339} , βL^{342} in the last NBD helix, and βI^{344} , βP^{350} , βL^{351} in the linker preceding CTD), and 2) eleven CTD residues: three hydrophobic residues (βL^{378} , βY^{381} in the helix-turn-helix motif (HTH), and βY^{458} in the last loop) and eight polar residues (βQ^{379} , βK^{382} , βQ^{385} , βQ^{411} , βR^{412} in HTH, and βE^{454} , βQ^{455} , βK^{469} in the last two helices of the protein). The polar residues contact the inhibitor mainly with their nonpolar moieties, so the interaction is predominantly hydrophobic. The side chains of βQ^{411} and βR^{412} form a hydrogen bond with the bicyclo carbonyl (O25) and pyrone (O19) oxygens, respectively. The pyrone forms a π - π stacking with βY^{458} . The β_{TP} binding site additionally contains αE^{399} , residue in HTH of α_{TP} , which makes a van der Waals contact with the AUR B O17 atom (>20 Å in β_E).

In this work, we carried out a computational characterization of the AUR binding sites with the aim of shedding new insights into the structural and energetic basis of inhibitor recognition for the future development of modulators of F₀F₁-ATP synthase activity. The bovine and human F₁ subcomplexes share high sequence identity (98% and 99% identity for α and β subunits, respectively), while the residues that form the AUR binding site are identical in the two species. Thus, we assume that the properties derived from the analysis of BtF₁ structure would largely reflect those of the human ortholog. Using molecular dynamics simulations and end-point binding free energy calculations, novel aspects of the AUR binding sites were revealed regarding intra- and intersubunit communications,

conformational trends, hot spot binding residues, and solvent sites that could be useful as pharmacophoric guides in virtual screening campaigns. In addition, analysis of bacterial sequences provided information on the conservation of the identified hot spot residues. This information could be relevant for the search for inhibitory molecules of this enzyme to treat human diseases or hinder the life cycle of pathogens.

2 Methods

Molecular dynamics simulations. MD simulations were performed with the AMBER 16 suite and the FF14SB force field (Maier et al., 2015; Case et al., 2016) using the crystal structures of bovine mitochondrial F₁-ATPase solved in the ground state (PDB ID: 2jdi (Bowler et al., 2007)) and complexed with AUR B (PDB ID: 1cow (van Raaij et al., 1996)). In both F₁ structures, the first 8 to 23 residues of the α and β subunits are missing, and the β subunits have not solved up to four residues at the C-terminus. To avoid adding artificial terminal charges, the first and last solved residues were capped with ACE and NME groups, respectively. In the ground state structure, segments 402–409 and 388–396 of B (α_{TP}) and E (β_E) chains, respectively, are not solved. These residues, corresponding to the turn segment of the HTH motif in each subunit, were modeled as loops using Modeller v9.20 (Šali et al., 1993). The γ subunit segments 45–76 and 87–208 are not solved in both F₁ structures. Hence, only residues 1–44 and 209–272, corresponding to the two large α -helices were included in the simulations. These helices remained stable along all trajectories, and the regions embedded in the catalytic hexamer maintained their conformation practically invariant with respect to the crystallographic structure (RMSD <0.5 Å over the backbone heavy atoms between the average MD and crystal structures). Simulations of the AUR complexes with F₁ from *E. coli* (PDB ID: 3oaa (Cingolani and Duncan, 2011)) and *Mycobacterium smegmatis* (PDB ID: 6foc (Zhang et al., 2019)) were also performed. AUR was docked on the crystal structures of these bacterial enzymes using BtF₁-AUR complex as a template. The conformations of the side chains exhibiting steric clashes with the inhibitor were modified to fit the closest conformation observed in BtF₁, using the Dunbrack 2010 rotamer library (Shapovalov and Dunbrack, 2011). In the case of missing residues, the corresponding terminal residues were blocked similarly to BtF₁. In the mycobacterium enzyme, the missing segments 42–46 and 109–113 of the three β subunits, both in the N-terminal domain, were modeled. Three 1- μ s replicas for each system were run, yielding a total simulation time of 12 μ s. Proteins were protonated at pH 7.4 using PDBfixer (Eastman et al., 2017). All nucleotides and Mg²⁺ ions were included. ATP and ADP parameters were taken from (Meagher et al., 2003). Using AMBER's tLeap, each protein was placed in a truncated octahedral box, initially spanning

12 Å further from the solute in each direction, and solvated using the TIP3P water model (Jorgensen et al., 1983). The hydrogen mass repartitioning scheme was implemented using the ParmEd (<https://github.com/ParmEd/ParmEd>), which allows the use of a 4 fs time step integration (Hopkins et al., 2015). The system was geometrically optimized using the steepest descent algorithm for 5,000 cycles to adjust the orientation of the solvent and remove local clashes. Initial velocities were assigned to get a 150 K distribution, slowly increasing the temperature up to 310 K in 0.8 ns in the NVT ensemble. The system was further equilibrated for 1 ns at 310 K in the NPT ensemble. Production was run in the NPT ensemble. Systems were simulated using periodic boundary conditions and Ewald sums (grid spacing of 1 Å) as implemented in the PMEMD module (Salomon-Ferrer et al., 2013) for treating long-range electrostatic interactions with a 9 Å cutoff for direct interactions (Darden et al., 1993). The same cutoff was applied to Lennard-Jones interactions. Temperature and pressure control was achieved using the Langevin thermostat with a collision frequency of 4 ps⁻¹ and the Berendsen barostat with a pressure relaxation time of 2 ps, respectively. The SHAKE algorithm was enabled to fix any bond involving hydrogen atoms (Ryckaert et al., 1977; Miyamoto and Kollman, 1992). Unless otherwise stated, no other constraints were used. Coordinates were saved every 10 ps AUR B topology and parameter files were generated with the antechamber suite and the general Amber force field (GAFF2) for organic molecules using AM1-BCC atomic charges (Wang et al., 2004). AUR parameters used are listed in Supplementary Table S1 in the Supplementary Material. Using the backbone heavy atoms, trajectory conformers were superimposed on the crystal structure of each AUR-binding site. Otherwise, the use of larger portions of the protein (e.g., complete F₁) introduced minor, although significant, local variations in the position of the binding residues. Trajectory analysis was performed with CPPTRAJ (Roe and Cheatham, 2013) and Chimera UCSF v16 (Pettersen et al., 2004) software packages. Protein structure representations were generated with ChimeraX v1.3 (Pettersen et al., 2021).

Aurovertin binding sites. AUR-binding residues at β_E and β_{TP} sites were defined as those within 5 Å from the inhibitor in the crystal structure of the BtF₁ complex. In both pockets, the same set of binding residues was found: βA^{338} , βI^{339} , βL^{342} , βI^{344} , βP^{350} , βL^{351} , βL^{378} , βQ^{379} , βY^{381} , βK^{382} , βQ^{385} , βQ^{411} , βR^{412} , βE^{454} , βQ^{455} , βY^{458} , βK^{469} . αE^{399} was additionally found at the β_{TP} binding site.

Cross-correlation analysis: The description of the dynamic movement of the system atoms and the extent of the dynamic correlation was calculated as a covariance between the pairwise fluctuations (Estabrook et al., 2005). The cross-correlation coefficient $c(i,j)$ was calculated using the following equation:

$$c(i, j) = \frac{\langle \Delta r_i \cdot \Delta r_j \rangle}{\langle \Delta r_i^2 \rangle^{1/2} \langle \Delta r_j^2 \rangle^{1/2}} \quad (1)$$

where Δr_i and Δr_j are the ensemble average displacement vectors of atoms i and j , respectively. Positively correlated motion implies that two atoms move in the same direction, whereas an anticorrelated motion implies the atoms move in the opposite direction. (Ichiye and Karplus, 1991).

Dihedral angle principal component analysis. Principal component analysis (PCA) is employed in MD as a data dimensionality reduction technique that converts a set of correlated motions into a set of orthogonal principal components containing the dominant trend of the protein's collective motions (Stein et al., 2006). To correctly separate the overall and internal motions (Altis et al., 2008), dihedral angle PCA (dPCA) was performed on the AUR binding site residues on the concatenated trajectories of each system, using CPPTRAJ (Roe and Cheatham, 2013). These angles were transformed to a linear metric coordinate space to avoid circularity problems, using the functions $\sin(x)$ and $\cos(x)$. Then, the 2N covariance matrix was calculated. The next step was the decomposition (diagonalization) of the covariance matrix, where the instantaneous linear correlations between variables were removed and the eigenvectors and eigenvalues were computed. The eigenvalues were arranged in a descending order.

Two-dimensional free energy landscapes (FEL) with the two first principal components, PC1 and PC2, were built with PyEMMA (Scherer et al., 2015), using the following equation:

$$F(x) = -k_B * T * \ln P(x) \quad (2)$$

where $F(x)$ is the x -coordinate free energy landscape, k_B is the Boltzmann constant, T is the absolute temperature and $P(x)$ is the x -coordinate probability distribution, taken as the two-dimensional histogram of PC1 and PC2.

Markov State Models (MSM). To quantify the relative abundance of visited conformations, MSM were constructed with PyEMMA (Scherer et al., 2015). As a first step, dPCA was applied over the MD trajectories. The resultant subspace of the first two principal modes was then discretized by creating a set of 1,000 conformational microstates using the k -means clustering method. The MD trajectories were encoded as a stochastic matrix based on the transition probabilities constructed using maximum likelihood and Bayesian estimation. Perron-cluster cluster analysis (Deuffhard and Weber, 2005) was implemented to group microstates into macrostates based on kinetic similarities.

Solvent-site identification and guided docking. Solvent sites for ethanol were determined using the MDMix method, as described elsewhere (Alvarez-Garcia and Barril, 2014; Avila-Barrientos et al., 2022). Three replicas of 20 ns each were run using the AUR-bound crystal structure, from which the two inhibitor molecules were removed. Conditions similar to those mentioned in the MD section were used, but with the following differences: the protein was embedded in a box of water/ethanol 80/20% v/v, and Cartesian restrictions of 0.1 kcal/mol Å² were

applied on the protein heavy atoms. After trajectories were aligned, density maps for probe atoms were obtained by building a static mesh of grids over the entire simulation box and counting the appearance of probe atoms in each grid during the trajectory. The observed appearance was converted into binding free energy (ΔG_{SS}) applying the Boltzmann relationship, considering the observed probe atom distribution and the expected distribution in bulk solvent at 1.0 M. Solvent sites were filtered by imposing an energy threshold of 1 kcal/mol. Solvent sites were used as pharmacophoric elements to dock AUR and related compounds at the AUR binding site using rDock (Ruiz-Carmona et al., 2014), as described elsewhere (Avila-Barrientos et al., 2022). Ligand protonation states were generated with Open Babel v. 2.3.1 (O'Boyle et al., 2011).

Relative binding free energy prediction. Relative binding free energies for the complex (G_{PL}) and the free reactants (G_P , G_L) were calculated using the MM-PBSA (Molecular Mechanics Poisson-Boltzmann Surface Area) single-trajectory approach (Wang et al., 2019). No convergence was observed using the two or three-trajectory approaches. Free energy changes (ΔG_{PB}) and their decomposition per binding residue were calculated with the MMPBSA. py script (Miller et al., 2012), according to:

$$\begin{aligned} \Delta G_{PB} &= \langle G_{PL} - G_P - G_L \rangle = \Delta H - T\Delta S \\ &= \Delta E_{MM} + \Delta G_{sol} - T\Delta S_{conf} \end{aligned} \quad (3)$$

$$\Delta E_{MM} = \Delta E_{bond} + \Delta E_{ele} + \Delta E_{vdW} \quad (4)$$

$$\Delta G_{sol} = \Delta G_{PB} + \Delta G_{np} \quad (5)$$

$$\Delta G_{np} = \gamma * SASA + b + E_{disp} \quad (6)$$

where ΔE_{MM} is the potential energy change in vacuum, ΔG_{sol} is the solvation energy, and $T\Delta S_{conf}$ is the conformational entropy change. ΔE_{MM} is further divided into bonded (ΔE_{bond}), electrostatic (ΔE_{ele}) and van der Waals (ΔE_{vdW}) energies changes. ΔG_{sol} is the sum of the polar solvation contribution, calculated using the Poisson-Boltzmann model, and the non-polar contribution (ΔG_{np}), calculated as the sum of the free energy of the cavity and the van der Waals interactions between the solvent and the solute as a linear relationship to the solvent-accessible surface area (SASA). Smooth surface (sasopt = 2) was used, with surface tension γ and offset correction b values of 0.0378 kcal/molÅ² and 0.5692 kcal/mol, respectively (Ye et al., 2010). E_{disp} is the attractive interaction between the solute and the solvent (Tan et al., 2007). The atom-type/charge-based radii were used (Tan et al., 2006). $T\Delta S$ contains the entropies arising from the particle number change ($T\Delta S_{r,t}$) and the freezing of rotatable bonds ($T\Delta S_{conf}$). The first contribution has a penalty of ~3 kcal/mol (Amzel, 1997; García-Hernández and Hernández-Arana, 1999); the second is usually calculated with the normal mode analysis or the quasi-harmonic approximation (Chang et al., 2005; Wang et al., 2019), although this term was not calculated in this work because of the large system size. The calculations were performed with 400 frames spaced every 6 ns. Dielectric constants for solvent and solute were set to 80 and 2,

respectively, using an ionic strength of 150 mM. The required topology files were created using the ante-MMPBSA.py script implemented in AmberTools (Case et al., 2016).

Sequence analysis of the AUR binding site. Bacterial ATP synthase β subunits sequences were retrieved from the UniProt database (Bateman et al., 2021). Jalview2 (Waterhouse et al., 2009) was used to curate the database, excluding redundant sequences (identity <100%). The curated database was used to generate a multiple sequence alignment with Clustal Omega (Sievers et al., 2011). Sequence logos were generated using the Weblogo3 server (Crooks et al., 2004). Virtually the same results were obtained using 98% or 99% redundancy sequence identity cutoffs.

3 Results

Protein-inhibitor interaction patterns. To carry out a computational characterization of the interaction of F_1 with AUR B (AUR⁺), we used the crystal structure of the bovine subcomplex bound to two inhibitor molecules (van Raaij et al., 1996). As the reference structure of the subcomplex without AUR B (AUR⁻), the so-termed “ground state” structure was used (Bowler et al., 2007). This structure has the particularity of being solved bound to nucleotides but in the absence of any inhibitor, so it is considered an accurate representation of the catalytic intermediate in the direction of hydrolysis. The AUR-bound and “ground state” structures of BtF₁, like most of those experimentally solved so far, correspond to the catalytic dwell in a 120° rotary substep (Sobti et al., 2021). Therefore, the following analysis circumscribed to the study of the conformational behavior of this metastable state.

To characterize the dynamics of the protein-inhibitor interactions, three MD replicates of 1 μ s each were run for BtF₁ bound to the two AUR B molecules, a time span that is two to three orders of magnitude smaller than the actual enzyme rotation time length (Sekiya et al., 2017). An autocorrelation analysis of the backbone dihedral angles indicated that relaxation of both binding sites occurred within the first 0.2 μ s of simulation (Supplementary Figure S1A). Faster convergence was observed for RMSD (Supplementary Figure S1B). Therefore, the analysis was performed on a concatenated trajectory of the last 0.8 μ s of each replica. Similar interaction patterns with the inhibitor were observed in β_{TP} and β_E (Figure 2C and Supplementary Figure S2). βQ^{379} , βE^{454} and βK^{469} lost interaction with the inhibitor during the simulation (gray residues in Figure 2B), with cumulative contact frequencies <0.25 (Figure 2C). Therefore, these residues were excluded from further analysis. The other 14 β -subunit residues showed cumulative contact frequencies >0.8. A large conformational variability was observed in α_{TP} . In two trajectories, HTH of this subunit approached AUR B, and four additional residues (αL^{392} , αE^{393} , αA^{395} , αQ^{396}) persistently contacted the inhibitor (Figures 2B,C). In the other trajectory, HTH stayed away from AUR, and

even the interaction with αE^{399} was completely disrupted. On the average, each of these four α_{TP} residues had a cumulative contact frequency >0.5, thus, together with αE^{399} , they were considered AUR-binding residues.

Overall, the poses and interaction modes of AUR B observed in the crystal structure were kept at both binding sites during the MD trajectories. The hydrogen bonds between βR^{412} -O19 and βQ^{411} -O25 remained formed throughout the simulations, except at the β_E site, where the βQ^{411} -O25 bond was broken in the last 0.3 μ s of one trajectory because of a partial ligand dissociation (Figures 3A,B and Supplementary Figure S3A,B). Recurringly, αE^{399} and βR^{412} , which are 8–10 Å from each other in the crystal structures, formed a salt-bridge at the β_{TP} site (Figure 3C). This contact, either mono or bidentate, was present ~70% and ~90% for AUR⁺ and AUR⁻, respectively. The interaction between βQ^{455} and αE^{399} was observed ~60% of the time for AUR⁻, whereas the inhibitor completely blocked this interaction. Although sporadically (~2%), the interaction between βR^{408} and αE^{399} , residues that are ~10 Å from each other in the crystal structure, was only observed for AUR⁻. This hydrogen-bond network transiently occluded the β_{TP} site, generating a steric hindrance for AUR access. Interestingly, βR^{408} , βR^{412} , βQ^{455} , and αE^{399} are part of a cooperative hydrogen bond network (which includes βL^{342} and αQ^{396}) that stabilizes the interaction between CTD of α_{DP} and β_{DP} , as illustrated in Supplementary Figure S3C. Consistent with this, a dynamic cross-correlation analysis indicated AUR decouples the side chain movements of the residues that form this network, as shown in Figures 3D,E. Thus, these results suggest that α_{TP} and β_{TP} exhibit a clear trend to interact with each other towards the adoption of an α_{DP}/β_{DP} -like conformation. The importance of this hydrogen-bond network has been demonstrated through directed mutagenesis experiments, showing that its disturbance affects the catalytic activity and can even prevent the assembly of the enzyme (Mao et al., 2008). These mutations do not change the affinity for the nucleotides (Ichikawa et al., 2005; Mao et al., 2008). Therefore, AUR B seems to hinder the interaction between the CTD of α_{TP} and β_{TP} , suggesting that the action of this inhibitor is partially related to the interruption of the dynamic communication of conformational changes between these subunits. Consistent with this, inhibitors like IF1, ϵ , ζ , or glycomacrolides prevent the formation of the CTD interactions established at the α_{DP} and β_{DP} interface (Cabezón et al., 2003; Cingolani and Duncan, 2011; Morales-Rios et al., 2015; Reisman et al., 2022).

Conformational dynamics of the AUR binding sites. Principal component analysis was performed on dihedral angles to assess conformational fluctuations of the AUR binding sites. Figure 4 shows the conformational landscape of the β_{TP} binding site for the first two principal modes (those capturing the largest conformational dispersion). The β_E results are shown in Supplementary Figure S4. An analysis of backbone dihedral angles revealed two basins of attraction

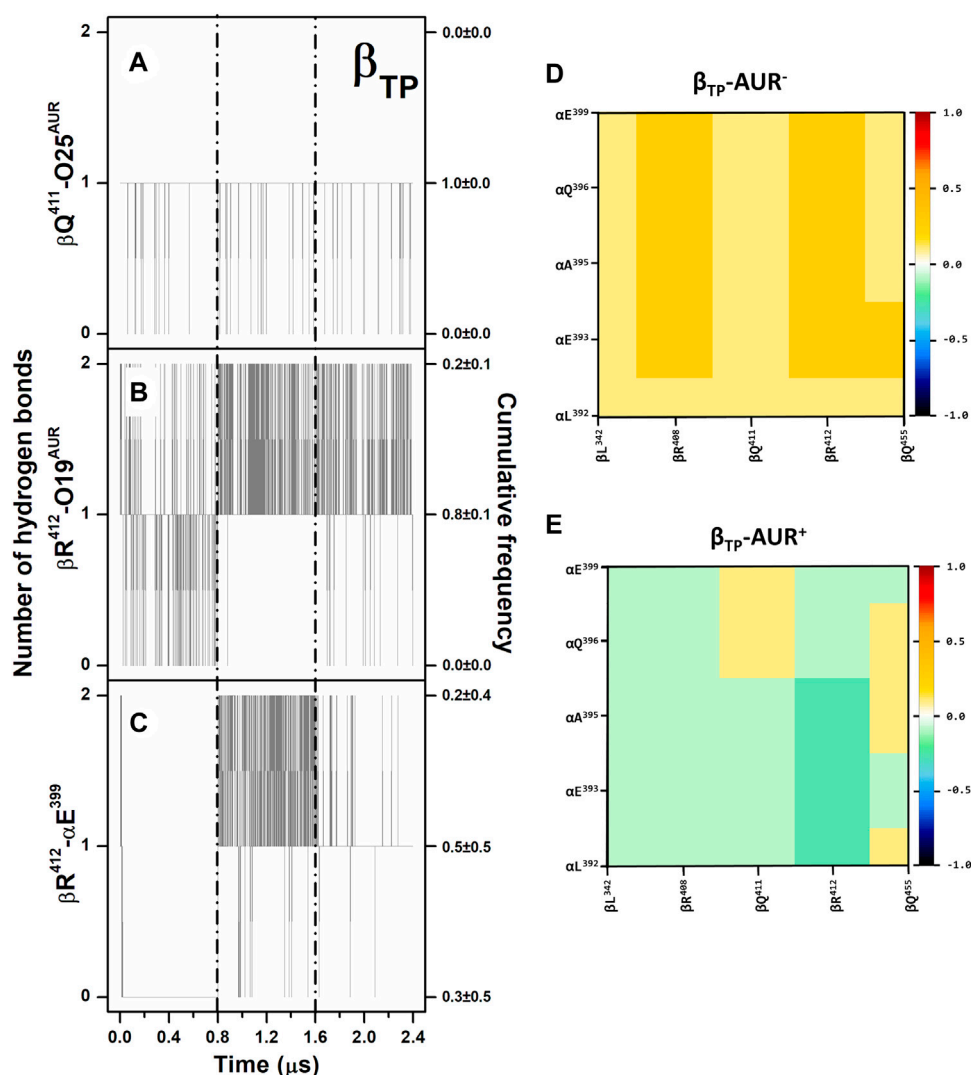


FIGURE 3

Hydrogen bonding in β_{TP} -AUR $^{+}$ and correlated motions of α_{TP} and β_{TP} CTD residues. **(A and B)** Protein-inhibitor hydrogen bonds. **(C)** α_{TP} - β_{TP} hydrogen bond. Data for the three concatenated 1- μ s replicas are shown, after subtracting the first 0.2 μ s of simulation from each one. The trajectories of each replica are delimited by dashed lines. Cumulative frequencies refer to the total fraction of time each number of hydrogen bonds was observed in the simulations. **(D and E)** Dynamic cross-correlation maps of α_{TP} and β_{TP} CTD residues, calculated over side chain atoms around their mid-positions for 2.4- μ s MD simulations in the absence and presence of AUR.

(S1 and S2) for AUR $^{-}$ that, based on an inspection of the conformers of each state, vary significantly only in the ψ angle of βI^{344} (Figure 4A). S1 adopted $\psi = 120 \pm 13^{\circ}$, a conformation like that observed in the two crystal structures of BtF $_1$, and S2 distributed around $\psi = 57 \pm 11^{\circ}$. S1 was less populated than S2 in β_{TP} and nearly equipopulated in β_E (Supplementary Figure S4A). The inhibitor decreased the overall dynamics of both sites to a similar value (Figure 5A), populating the same single attraction basin equivalent to S1 (Figure 4B and Supplementary Figure S4B), that is, the crystal conformer. Because of the greater mobility of the ligand-free binding site in β_E , the inhibitor induced larger backbone stiffness

compared to the β_{TP} site. The five α_{TP} residues also formed a single attraction basin for AUR $^{+}$ and three basins for AUR $^{-}$ (Supplementary Figure S5). A side chain dihedral angle analysis revealed a more complex conformational behavior. To discern the underlying collective movements, a MSM analysis was performed. These kinetic models describe the conformational dynamics of biomolecular systems in terms of transition rates between conformational states (Pande et al., 2010; Husic and Pande, 2018). As shown in Figures 4C,D and Supplementary Figure S4C,D, the conformational landscape of the side chains at the β_{TP} binding site is composed of several attraction basins. The number of attraction basins and the

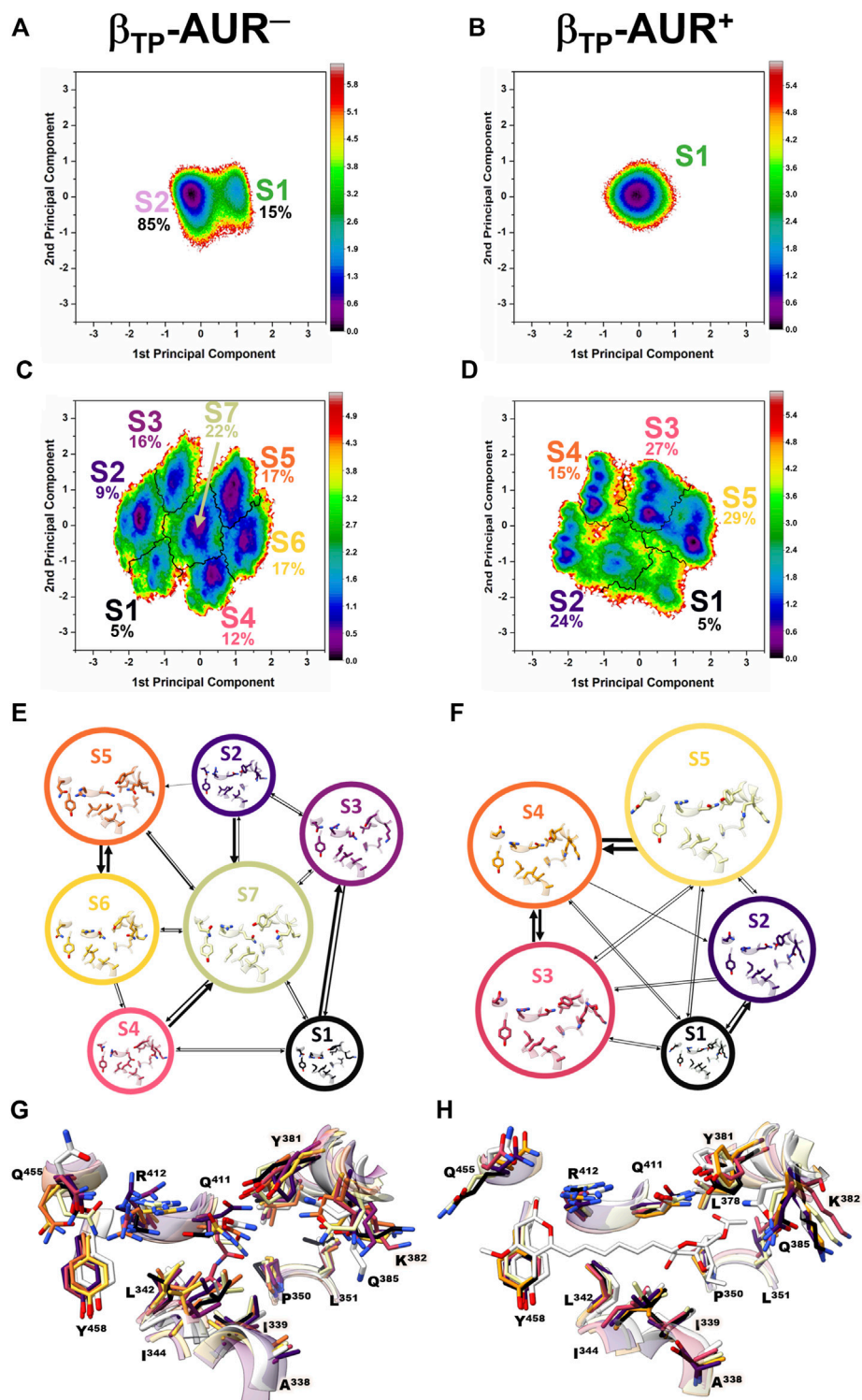


FIGURE 4

Dihedral angle free energy landscapes (FEL) for the AUR binding site residues in β_{TP} . FEL (in $k_B T$ units) were obtained from a dPCA projected onto the first two principal components in the absence (left column) and presence (right column) of the inhibitor. (**A and B**) Backbone dPCA. One and two metastable conformational states were observed for AUR^+ (S1) and AUR^- (S1, S2), respectively. The percentage of cumulative frequency is indicated. The main difference between S1 and S2 was the ψ angle value of I³⁴⁴. (**C and D**) Side chain dPCA. The black lines delimit the macrostates identified through a Markov-state model analysis. (**E and F**) Network transition pathway of the Markov-state model. The thickness of the connecting arrows is proportional to the transition probability. (**G and H**) Superimposition of representative conformations for each attraction basin in (**E and F**). Macrostates were labeled S1, S2 and so on from lowest to highest occupancy.

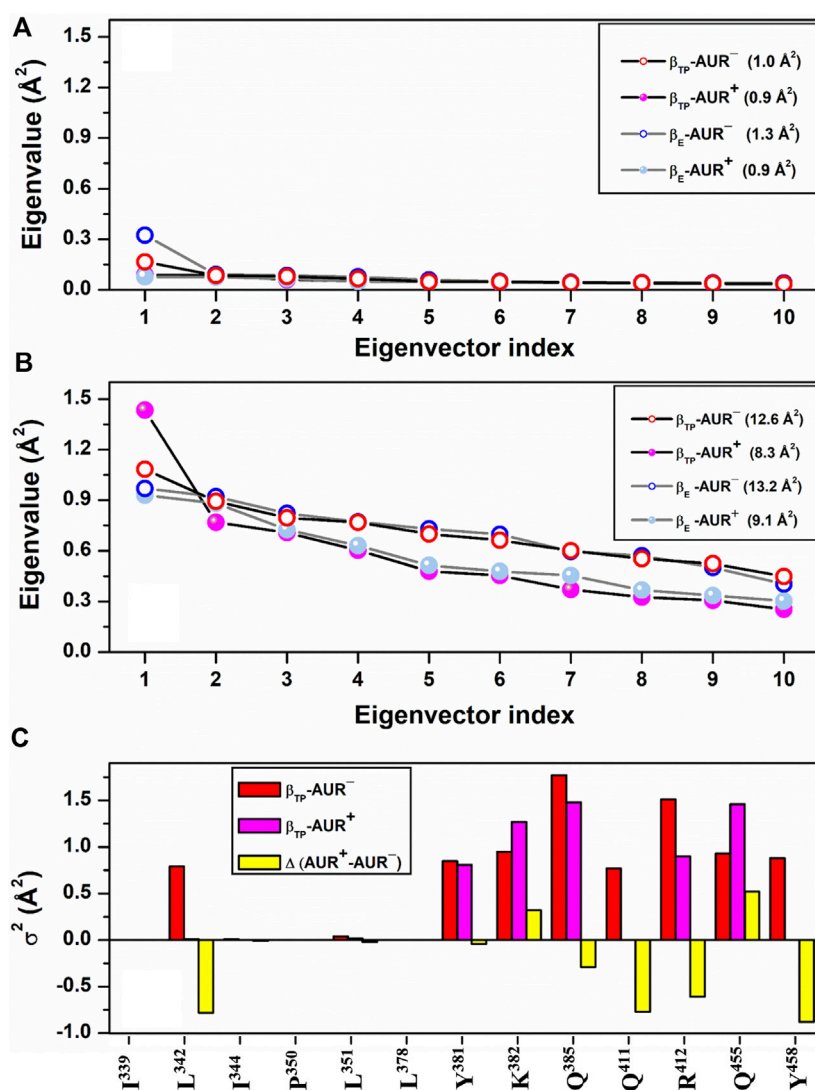


FIGURE 5

dPCA scree plots for AUR binding residues. The eigenvalue distributions for the first ten eigenvectors for backbone and side chain dihedral angles are shown in (A) and (B), respectively. Values in parentheses indicate the total variance for the indicated system. (C) Cumulative variance per residue (σ^2) of side chains at the β_{TP} site. Δ (AUR⁺-AUR⁻) is the σ^2 difference in presence minus in absence of the inhibitor. Values correspond to 70% of the total variance.

total variance decreased with AUR B (Figure 5B). In β_{TP} , the inhibitor completely froze the side chains of β L³⁴², β Q⁴¹¹, and β Y⁴⁵⁸, while the side chains of β I³³⁹, β I³⁴⁴, β P³⁵⁰, β L³⁵¹, and β L³⁷⁸ were already frozen without the inhibitor (Figures 4E-H and Figure 5C). β Q³⁸⁵ and β R⁴¹² partially decreased their mobility with AUR B, and the peripheral residues β K³⁸² and β Q⁴⁵⁵ slightly increased it. Finally, regardless of the presence of AUR, Y³⁸¹ had the same mobility. A similar behavior was observed for β_E (Supplementary Figure S6). Overall, these results showed that the AUR binding site is preformed in both catalytic subunits, undergoing relatively minor rearrangements and conformational constraints upon

inhibitor binding, although the reduction in mobility was somewhat greater at the β_E site. To contrast these results with experimental data, we analyzed the conformational variations between solved BtF₁ structures (resolution better than 3.5 Å). As shown in Supplementary Figure S7A, 28 structures retrieved from the PDB closely overlapped each other at the AUR binding site in β_{TP} (RMSD < 0.8 Å over the backbone heavy atoms). Thus, regardless of crystallization conditions, bound inhibitor, and/or the occupancies at the nucleotide binding sites, the backbone conformation at the AUR binding site is practically invariant. In addition, when projected onto the FEL for

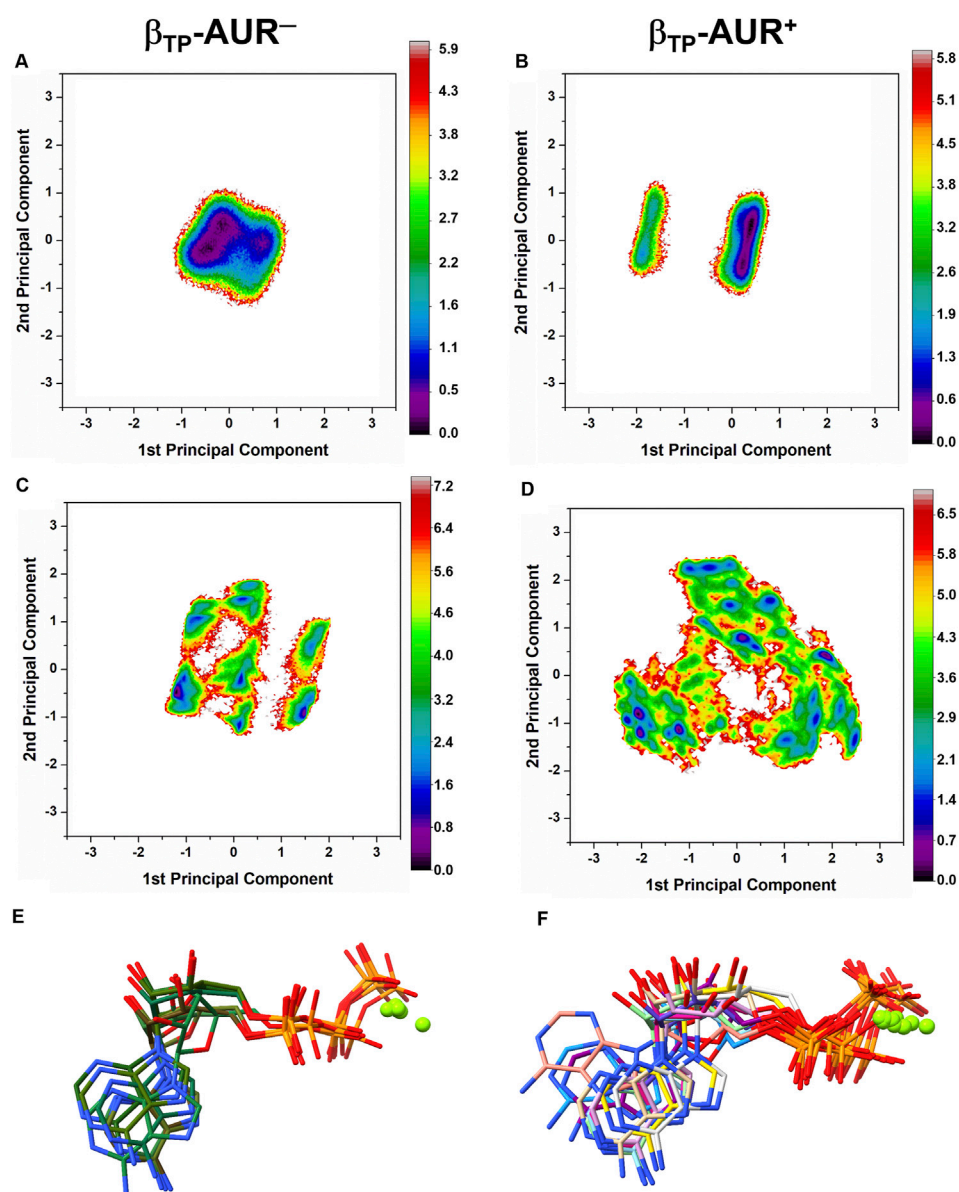


FIGURE 6

Dihedral angle free energy landscapes (FEL) for the nucleotide binding site in β_{TP} . (A) Backbone FEL for AUR^- . (B) Backbone FEL for AUR^+ . (C) Side chain FEL for AUR^- . (D) Side chain FEL for AUR^+ . FEL (in $k_B T$ units) were obtained from a dPCA projected onto the first two principal components in the absence (left column) and presence (right column) of the inhibitor. Residues with χ angles within 5 Å of the nucleotide in β_{TP} (V^{160} – V^{164} , R^{189} , T^{190} , R^{260} , Y^{311} , Y^{345} , P^{346} , Q^{416} , F^{418} , F^{424} , T^{425}) were included in the analysis. (E) and (F) Representative MgATP conformations for AUR^- and AUR^+ , respectively. Magnesium atoms are shown as green spheres.

β_{TP} - AUR^- , most of the crystal structures fell within the most visited macrostate region, while two of them resembled the second largest macrostate (Supplementary Figure S7B). Finally, it is noteworthy that the shift of the α_{TP} HTH towards the AUR binding site observed in our simulations is present, although less pronounced, in four solved BtF₁ structures in complex with IF1 (Gledhill et al., 2007b; Bason et al., 2014, 2015).

Effects of AUR on catalytic sites. *In vitro* studies have shown that AUR exerts a mild positive cooperative effect on the catalytic sites of BtF₁ and EcF₁ (Issartel et al., 1983b; Issartel and Vignais, 1984). Perhaps the best solved measurement of the reciprocal binding effect of AUR and substrate nucleotides was made on the isolated β subunit (Issartel and Vignais, 1984; van Raaij et al., 1996; Johnson et al., 2009). The inhibitor increases ADP/ATP affinities by 3–7-fold (~ 0.4 – 1.1 kcal/mol of Gibbs free energy).

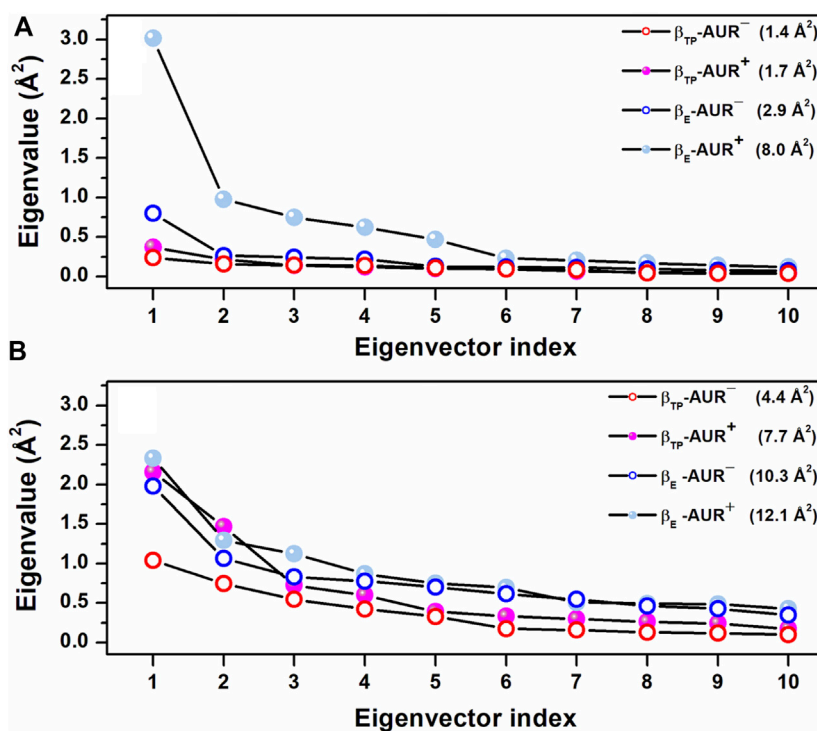


FIGURE 7

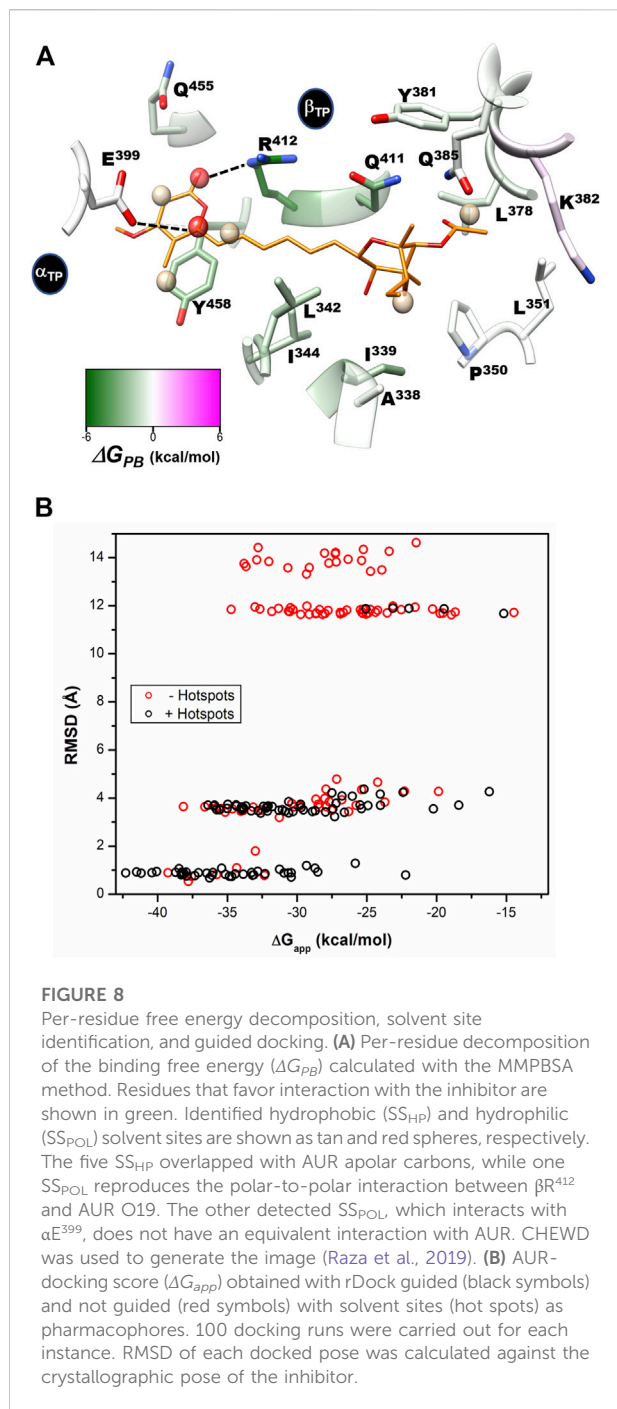
Scree plots obtained from dPCA for nucleotide binding residues in β_{TP} . (A) Backbone dihedral angles. (B) Side chain dihedral angles. The eigenvalue distributions for the first ten eigenvectors are shown. The values in parentheses indicate the total variance for the corresponding system. Residues with χ angles within 5 Å of the nucleotide in β_{TP} (V^{160} - V^{164} , R^{189} , T^{190} , R^{260} , Y^{311} , Y^{345} , P^{346} , Q^{416} , F^{418} , F^{424} , T^{425}) were included in the analysis.

Likewise, the AUR-like molecule citreoviridin decreases K_m in F_1 from *Trypanosoma cruzi* (Cataldi de Flombaum and Stoppani, 1981). Thus, in addition to acting as a physical blocker, AUR has effects on F_1 beyond its own binding sites. To investigate these effects, we analyzed the conformational properties of the nucleotide binding sites in β_{TP} and β_E . Figure 6 shows the conformational landscapes for the backbone and side chain dihedral angles of the nucleotide binding residues in β_{TP} . Strikingly, more complex landscapes and larger mobilities were observed with AUR B in β_{TP} (Figures 6A–D and Figure 7). Along with this, ATP mobility increased significantly for AUR⁺ (Figures 6E,F). Interestingly, even without nucleotide in the catalytic site, an increased mobility in β_E was observed for AUR⁺ compared to AUR⁻ (Figure 7 and Supplementary Figure S8). Overall, these results are consistent with a favorable conformational entropy contributing to the increase in nucleotide affinity elicited by the inhibitor.

Solvent site identification and free energy calculations. To investigate the energetic relevance of AUR binding site residues, we performed MD simulations in an ethanol/water solvent box using the MDMix method (Alvarez-Garcia and Barril, 2014). In brief, this approach allows the organic solvent to diffuse unbiasedly over the protein surface through a process governed only by the time evolution of the atomic energies and degrees of freedom of the

system. Those regions of the protein that interact favorably with the cosolvent will define solvent sites (SS) characterized by higher occupancies than in the bulk solvent, from which it is possible to calculate the free energy of interaction (ΔG_{SS}) at each site. Active and allosteric sites usually define SS, since they have the appropriate stereochemistry to form stable interactions with organic molecules (Alvarez-Garcia and Barril, 2014; Arcon et al., 2017). MDMix has been valuable not only in helping to determine the dominant residues or “hot spots” in molecular recognition (Arcon et al., 2017), but also in guiding the discovery and design of new pharmacological molecules, both orthosteric and allosteric (Rachman et al., 2020; Talibov et al., 2021; Avila-Barrientos et al., 2022).

As revealed from the trajectories without the inhibitor, the AUR binding site tended to be occluded because of the propensity to form hydrogen bonds between α_{TP} and β_{TP} residues. Therefore, to characterize the solvation of the conformation competent to bind the inhibitor, harmonic constraints were applied to all protein heteroatoms. Figure 8 shows SS determined for the β_{TP} site from the average of three independent trajectories, each 20 ns long. Two types of SS, one for the methyl group and another for the hydroxyl group of ethanol, were calculated as probes for hydrophobic (SS_{HP}) and polar (SS_{POL}) interactions, respectively. βA^{338} , βI^{339} , βL^{342} , βI^{344} ,

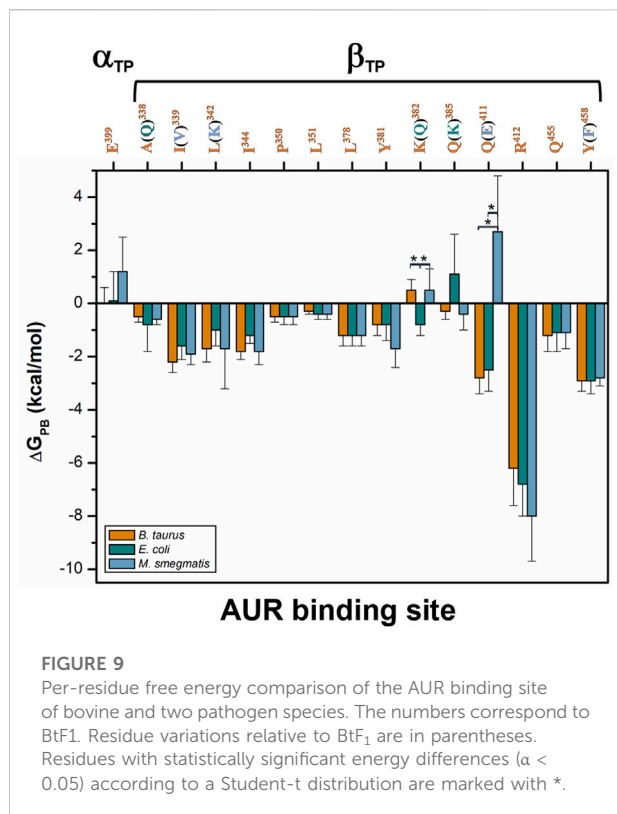


βL^{351} , βL^{378} , βY^{381} , βK^{382} , βR^{412} , βQ^{455} and βY^{458} , all of them involved in AUR binding, stabilized the five SS_{HP} detected (Figure 8A). Three SS_{HP} were observed in the pyrone binding region and another two in the bicyclo region of AUR. βY^{458} simultaneously stabilized three SS_{HP} , highlighting the importance of this residue in the interaction with organic molecules. αE^{399} and βR^{412} stabilized the two detected SS_{POL} . The one near αE^{399} did not reproduce any equivalent interaction with AUR B. In contrast, the other SS_{POL} replicated

the interaction between βR^{412} and O19 of AUR B, whereas no SS_{POL} was solved for the βQ^{411} -O25 interaction. Interestingly, molecular docking experiments on BtF₁ guided by all six SS emulating the interaction with AUR B (i.e., excluding the one close to αE^{399}) improved the ability to predict the crystal position of the inhibitor (Figure 8B). In the absence of SS information, the docking success rate for predicting the correct AUR B position was only 39%. Relative to the crystal binding mode, the pyrone appeared inverted in most poses. In contrast, the success rate increased to 91% with the use of SS information. Similar results were observed with citreoviridin and asteltoxin, two AUR-like compounds (data not shown). Less SS were reproduced at the β_E site. The two SS_{POL} in β_{TP} were not solved (Supplementary Figure S9), suggesting the importance of the α subunit in defining the interaction.

To assess the per-residue energy contribution in the interaction with AUR B, the binding free energy (ΔG_{PB}) was calculated using the MMPBSA method (Wang et al., 2019). This approach combines molecular mechanics and a continuum solvation model to calculate the endpoint binding free energies (Equation 3) (Genheden and Ryde, 2015). The energy of the solute is calculated by the force field. Solvation free energy has two components, polar and nonpolar solvation energies (Equation 5). The first term is calculated by solving the Poisson-Boltzmann equation. In a broad sense, this means calculating the energy associated with transferring charges from the vacuum to the continuum. The second models the solute cavity formation and the non-electrostatic interactions between the solute and the continuum close to the cavity. This is usually calculated with an approximation based on surface area and a van der Waals dispersion term. In the single-path approach, structural changes associated with ligand binding are not considered, and conformational entropy is generally ignored, as it does not improve calculations (see further details in the Methods section) (Wang et al., 2018).

Based on reported K_d values, the experimental binding Gibbs free energy (ΔG_b) for AUR B with BtF₁ is 9.5 kcal/mol (Hong and Pedersen, 2008). Using $\epsilon = 2$, ΔG_{PB} values of -18.6 ± 4.6 and -16.3 ± 3.1 kcal/mol were obtained for the β_{TP} and β_E sites, respectively. These magnitudes are in reasonable agreement with the experimental one, considering the loss of roto-translational ($T\Delta S \sim -3$ kcal/mol (Amzel, 1997; García-Hernández and Hernández-Arana, 1999)) and conformational ($T\Delta S \sim 0.5$ kcal/mol per frozen rotatable bond) entropies, which were not included in the calculations. In contrast, with $\epsilon = 1$, $\Delta G_{PB} = 9.0 \pm 4.7$ and 7.1 ± 4.5 kcal/mol were obtained for the β_{TP} and β_E sites, respectively, which clearly underestimate the experimental binding strength. Regardless of the value used for the internal dielectric constant, the per-residue energy ranking remained constant. According to the results shown in Figure 9, the residues that most contributed to the binding free energy in β_{TP} were $\beta R^{412} > \beta Y^{458} \approx \beta Q^{411} > \beta I^{339} > \beta L^{342} \approx \beta I^{344} > \beta L^{378} \approx \beta Q^{455}$, which ranged between -6.2 ± 1.4 (βR^{412}) to 1.2 ± 0.6 (βQ^{455}) kcal/mol ($\epsilon = 2$). Similar ΔG_{PB} results were obtained for β_E (Supplementary Figure



S9). These eight residues, about half of the AUR binding site, can be considered as “hot spots” that primarily determine the affinity for the inhibitor. According to these calculations, the subsites to which the pyrone and bicyclo moieties bind contributed similarly to the overall affinity, while the linker region had a negligible contribution. Consistent with our results, *Bacillus* species such as *B. PS3* and *B. firmus* OF4 are naturally insensitive to this molecule, which has been attributed to the substitution of βR^{412} and βY^{458} by F and R, respectively (Saishu et al., 1983; Hicks and Krulwich, 1995). In contrast, AUR inhibits the F_0F_1 -ATP synthases of *E. coli*, *Rhodospirillum rubrum*, *Alcaligenes faecalis*, and *Paracoccus denitrificans* (Satre et al., 1979). The enzymes from these bacterial species retain the same set of eight BtF₁ hot spots for AUR binding (Figure 9). Mutational studies aimed at understanding the molecular recognition of AUR by F_0F_1 -ATP synthase are scarce. The substitution of the equivalent bovine βR^{412} in *E. coli* by Cys, His or Trp makes the enzyme insensitive to AUR, whereas these mutations elicit a loss of catalytic activity between 0 and 29% (Lee et al., 1989, 1991).

Comparison of binding energetics with bacterial enzymes. To compare the AUR B binding energetics of BtF₁ with that of pathogenic bacteria, ΔG_{PB} for the F₁ sectors of *E. coli* (EcF₁) and *M. smegmatis* (MsF₁) were calculated. The crystal structures of these bacterial enzymes have not been solved in complex with AUR

(Cingolani and Duncan, 2011; Zhang et al., 2019). Thus, AUR B was docked on these enzymes using the bovine complex as a template. Three MD replicates of 1 μ s each were performed for each bacterial system. The AUR binding sites of EcF₁ and MsF₁ have 79 and 71% sequence identity with BtF₁, respectively. Residues A³³⁸, K³⁸², and Q³⁸⁵ in BtF₁ are replaced by Q, Q, and K in EcF₁, respectively, while residues I³³⁹, L³⁴², Q⁴¹¹, and Y⁴⁵⁸ in BtF₁ are replaced by V, K, E, and F in MsF₁, respectively. Despite these changes, the energy profiles of the three species were similar to each other. (Figure 9) The K³⁸²Q and Q³⁸⁵K mutations between BtF₁ and EcF₁ exhibited almost complete compensatory effects, while the A³³⁸Q substitution produced no significant changes, which is consistent with the fact that the interaction with the inhibitor was mainly mediated by the C β atoms of both residues. Experimental K_d values show that AUR binds to BtF₁ and EcF₁ with similar strength (Issartel et al., 1983a; 1983b), which is consistent with the overall ΔG_{PB} values obtained herein (ΔG_{PB} values of 18.6 ± 4.6 vs. 16.6 ± 4.4 kcal/mol, respectively). Therefore, the AUR binding site appears unsuitable for designing molecules that can discriminate between EcF₁ and the mammalian enzyme. As for MsF₁, it has not been experimentally determined whether AUR (or any other related compound) inhibits it. ΔG_{PB} did not indicate energetic changes for the mutations I³³⁹V, L³⁴²K, and Y⁴⁵⁸F, showing the formation of equivalent hydrophobic contacts with the inhibitor in both enzymes. In fact, the polar moieties of K in MsF₁ and Y in BtF₁ did not contact AUR B. The largest energy variation was observed for the Q⁴¹¹E substitution. This behavior seems to arise from the loss of the hydrogen bond between Q⁴¹¹ and AUR B O25 in BtF₁, and the generation instead of an electrostatic repulsion with the glutamate carboxylate group in MsF₁. To minimize this repulsion, the AUR B bicyclo rotated during the simulations to allow O25 to be more exposed to the solvent. In agreement with this, a smaller ΔG_{PB} value of -12.8 ± 5.0 kcal/mol was obtained for MsF₁. In our simulations, AUR B remained at the β_{TP} -AUR site throughout the trajectories, while rapidly dissociating from the β_E site (data not shown). With these results, a weaker affinity of MsF₁ for AUR B could be hypothesized. Potentially, compounds could be sought that take advantage of the Q⁴¹¹E mutation to specifically recognize this bacterial enzyme.

Given the potential use of the AUR binding site as an antimicrobial target, we explored its sequence conservation in the Bacteria domain. Figure 10 shows a sequence logo built from 23,125 bacterial β -subunit sequences retrieved from the UniProt database. Only 3,409 sequences (~15%) contained the same eight residues that contribute most to AUR B affinity in BtF₁, including human pathogens from the genera *Coxiella*, *Escherichia*, *Haemophilus*, *Legionella*, and *Rickettsia*. While 12,511 sequences (~54%) have both R and Y/F at positions

412 and 458 of BtF₁, respectively, only 1,497 (~6%) sequences have these residues swapped. Based on experimental evidence, pathogenic species from genera *Staphylococcus*, *Streptococcus* and *Enterococcus*, which contain the latter sequences, should be insensitive to AUR, as proven in *Bacillus* PS3. Also, 7,297 (~32%) sequences, including species from genera *Brucella*, *Campylobacter*, *Clostridium*, *Corynebacterium*, *Helicobacter*, *Mycobacterium*, and *Vibrio*, have E instead of Q at position 411. Hence, just considering these three residue positions, ~6–~48% of the sequences would have an abolished or weakened affinity for AUR. Notably, P³⁵⁰, L³⁵¹, and L³⁷⁸ are nearly invariant. I³⁴⁴ is another largely conserved residue, with minor substitutions mainly by L and M. The basis for such high conservation of these residues is unclear.

4 Discussion

There is a long list of incurable diseases and multi-resistance microbes that are of global concern (Franco-Serrano et al., 2018; Vasan et al., 2019; Hoffman, 2020). Therefore, there is a pressing need to exploit new molecular targets to diversify treatments for these conditions. The malfunction of F₀F₁-ATP synthase is implicated in the development of multiple human diseases (Huang et al., 2008; Ahmad et al., 2013; Nesci et al., 2019; Patel et al., 2020). However, despite multiple efforts, no pharmacological modulator of this promising target has yet been approved for clinical treatment of noninfectious diseases.

In contrast, with the authorization of bedaquiline as an antitubercular drug, this enzyme was validated as a species-specific antimicrobial target (Nesci et al., 2019). The idea of using exogenous inhibitors of F₀F₁-ATP synthase to treat human diseases is not new. Encouraging results have been reported to arrest the progression of different tumor cell lines through the inhibition of this enzyme by polyphenols, aurovertins, and glycomacrolides (Duan et al., 2020; Wu et al., 2020; Reisman et al., 2022). In principle, exogenous inhibitor binding sites could also be targeted to treat other diseases in which F₀F₁-ATP synthase is involved, although further research is still needed on this.

To our knowledge, this is the first study aimed at characterizing one of the non-functional F₀F₁-ATP synthase allosteric pockets to explore its druggability. Our results showed that the two AUR binding sites share similar conformational properties and recognition patterns, although an overall examination of the binding free energy, solvent site and hydrogen bonding results suggests that the β_{TP} site corresponds to the experimentally reported high-affinity site (Issartel et al., 1983a; Issartel and Vignais, 1984). Analysis of the conformational dynamics indicated that both AUR binding sites are preformed, in agreement with the relative invariance of these sites observed in all the experimental structures of BtF₁ solved so far. Free energy calculations and solvent sites identification, two computational approaches, identified the same triad (R⁴¹², Y⁴⁵⁸, and Q⁴¹¹) as the most stabilizing residues for interaction with the inhibitor, results that are consistent with experimental site-directed mutagenesis data and with the different AUR sensitivities that enzymes of various species have (Lee et al., 1989). These residues could therefore be used as primary hot spots in drug design campaigns. Natural aurovertins differ from each other in their pyrone, bicyclo and/or linker substituents (Hong and Pedersen, 2008; Patel et al., 2020). Unfortunately, not enough experimental binding data have been reported so far to establish a quantitative structure-activity relationship for these inhibitors. Our simulations revealed that, in the catalytic dwell conformation, there is a clear interaction trend between β_{TP} and α_{TP} CTD residues that had not been reported before. This tendency, partially interrupted by AUR, seems to be in the formation pathway of a network of hydrogen bonds established between α_{DP} and β_{DP} that, according to mutational studies (Mao et al., 2008), is relevant for the correct functioning of the enzyme. Besides acting as a steric blocker of the propagation of protein conformational changes, AUR exerts long-range effects, increasing the conformational flexibility of the side chains and the nucleotide in the active site of the same catalytic subunit. These observations are consistent with experimental cooperative affinity effects between the inhibitor and the substrates (Issartel et al., 1983a; Issartel and Vignais, 1984).

Experimental characterization of AUR binding to F₁ or entire F₀F₁-ATP synthase has been challenging, and

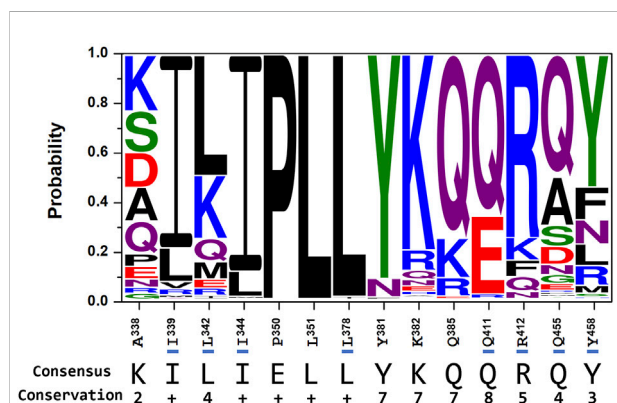


FIGURE 10

Conservation of the AUR binding site in bacterial FOF₁-ATP synthases. Residues (and numbering) on the x-axis correspond to the bovine sequence. Residues that, based on ΔG_{PB} calculations in Figure 9, contribute one or more kcal/mol of favorable binding free energy in BtF₁ are underlined in blue. The consensus sequence is also shown. The **Conservation** row corresponds to a scale ranging from 0 (null conservation) to 10 (= +, complete conservation of physicochemical properties of the amino acid group) as defined in (Livingstone and Barton, 1993). Multiple sequence alignment of 23,125 entries was performed with Clustal Omega (Sievers et al., 2011). Logos were generated using the Weblogo3 server (Crooks et al., 2004).

numerous aspects of the inhibition mechanism remain to be unveiled. Although the crystal structure revealed two molecules of AUR B bound to one F_1 , determination in solution of the stoichiometry (Verschoor et al., 1977; Issartel et al., 1983b; Johnson et al., 2009), binding affinities (Hong and Pedersen, 2008; Patel et al., 2020), and cooperative effects with the catalytic sites (Chang and Penefsky, 1973; Verschoor et al., 1977; Issartel and Vignais, 1984) has been challenging, with reported data varying depending on the conditions and measurement techniques, and which can be well described using different inhibition models (Johnson et al., 2009). In this sense, new experiments could be conceived based on the computational results presented here. For instance, mutations of key residues would be useful in improving our understanding of the mechanism of inhibition.

Free energy results for the interaction between AUR and F_1 from two bacterial species shed new light on the possibilities of using the AUR binding site as an antimicrobial target. Although the overall identity between the BtF_1 and EcF_1 AUR binding sites is ~80%, the eight energetically relevant residues for inhibitor binding are completely conserved. This conservation is consistent with the similar affinity values measured both *in silico* and *in vitro* for the two species. This suggests that the AUR binding site in EcF_1 might not be a good target for the development of species-specific antibiotics. By extension, a similar conclusion can be suggested for *Coxiella*, *Haemophilus*, *Legionella*, and *Rickettsia* pathogens which cause Q fever, respiratory track, legionellosis, and Rocky Mountain spotted fever diseases, respectively. In contrast, the identity of the eight most important binding residues between BtF_1 and MsF_1 is 50%, which, according to the simulations, weakens the affinity and modifies the binding pose of AUR B. Indeed, these results are not unexpected, as mitochondria are accepted to have originated from an α -protobacteria-like ancestor (Roger et al., 2017; Fan et al., 2020), and *E. coli* is a γ -protobacteria. *M. smegmatis* is a more distantly related actinobacteria. Although it is unknown whether AUR inhibits MsF_1 , this difference in composition could be useful for the development of species-specific antimicrobial drugs to treat tuberculosis and other communicable diseases such as brucellosis (*Brucella sp.*), botulism (*Clostridium botulinum*), cholera (*Vibrio cholera*), and diphtheria (*Corynebacterium diphtheriae*). An analysis of the AUR binding site of all bacterial sequences reported so far suggests that a significant number of species are insensitive to this class of inhibitor, and that varying degrees of affinity strength are likely to exist. Overall, our study lays the groundwork for structure-based drug design targeting the AUR binding site to treat human diseases in which F_0F_1 -ATP synthase is centrally involved, or for the development of new types of antibiotics.

Data availability statement

The original contributions presented in the study are included in the article/Supplementary Materials, further inquiries can be directed to the corresponding author.

Author contributions

Conceptualization, LC-V and EG-H; methodology, all authors; formal analysis, all authors; investigation, LC-V, PM-E; writing—original draft preparation, LC-V and EG-H; writing—review and editing, all authors; funding acquisition, EG-H and HR-R. All authors have read and agreed to the published version of the manuscript.

Funding

LC-V is student from Programa de Doctorado en Ciencias Bioquímicas, Universidad Nacional Autónoma de México (UNAM), and received fellowship No. 508395 from CONACyT, México. PM-E received a postdoctoral fellowship from Universidad Nacional Autónoma de México (UNAM). This work was partially supported by UNAM-DGAPA PAPIIT grant IN206221 to EG-H and IN219022 to HR-R.

Conflict of interest

The authors declare that the research was conducted in the absence of any commercial or financial relationships that could be construed as a potential conflict of interest.

The reviewer AM declared a shared affiliation with the author HR-R to the handling editor at the time of the review.

Publisher's note

All claims expressed in this article are solely those of the authors and do not necessarily represent those of their affiliated organizations, or those of the publisher, the editors and the reviewers. Any product that may be evaluated in this article, or claim that may be made by its manufacturer, is not guaranteed or endorsed by the publisher.

Supplementary material

The Supplementary Material for this article can be found online at: <https://www.frontiersin.org/articles/10.3389/fphar.2022.1012008/full#supplementary-material>

References

- Abrahams, J. P., Buchanan, S. K., Van Raaij, M. J., Fearnley, I. M., Leslie, A. G. W., and Walker, J. E. (1996). The structure of bovine F1-ATPase complexed with the peptide antibiotic efrapeptin. *Proc. Natl. Acad. Sci. U. S. A.* 93, 9420–9424. doi:10.1073/pnas.93.18.9420
- Abrahams, J. P., Leslie, A. G. W., Lutter, R., and Walker, J. E. (1994). Structure at 2.8 Å resolution of F1-ATPase from bovine heart mitochondria. *Nature* 370, 621–628. doi:10.1038/370621a0
- Ahmad, Z., Okafor, F., Azim, S., and Laughlin, T. F. (2013). ATP synthase: A molecular therapeutic drug target for antimicrobial and antitumor peptides. *Curr. Med. Chem.* 20, 1956–1973. doi:10.2174/0929867311320150003
- Altis, A., Otten, M., Nguyen, P. H., Hegger, R., and Stock, G. (2008). Construction of the free energy landscape of biomolecules via dihedral angle principal component analysis. *J. Chem. Phys.* 128, 245102. doi:10.1063/1.2945165
- Alvarez-Garcia, D., and Barril, X. (2014). Molecular simulations with solvent competition quantify water displaceability and provide accurate interaction maps of protein binding sites. *J. Med. Chem.* 57, 8530–8539. doi:10.1021/jm5010418
- Amzel, L. M. (1997). Loss of translational entropy in binding, folding, and catalysis. *Proteins* 28, 144–149. doi:10.1002/(sici)1097-0134(199706)28:2<144::aid-prot2>3.0.co;2-f
- Arcon, J. P., Defelipe, L. A., Modenutti, C. P., López, E. D., Alvarez-Garcia, D., Barril, X., et al. (2017). Molecular dynamics in mixed solvents reveals protein–ligand interactions, improves docking, and allows accurate binding free energy predictions. *J. Chem. Inf. Model.* 57, 846–863. doi:10.1021/acs.jcim.6b00678
- Avila-Barrientos, L. P., Cofas-Vargas, L. F., Agüero-Chapin, G., Hernández-García, E., Ruiz-Carmona, S., Valdez-Cruz, N. A., et al. (2022). Computational design of inhibitors targeting the catalytic β subunit of *Escherichia coli* FOF1-ATP synthase. *Antibiotics* 11, 557. doi:10.3390/antibiotics11050557
- Bason, J. V., Montgomery, M. G., Leslie, A. G. W., and Walker, J. E. (2015). How release of phosphate from mammalian F1-ATPase generates a rotary substep. *Proc. Natl. Acad. Sci. U. S. A.* 112, 6009–6014. doi:10.1073/pnas.1506465112
- Bason, J. V., Montgomery, M. G., Leslie, A. G. W., and Walker, J. E. (2014). Pathway of binding of the intrinsically disordered mitochondrial inhibitor protein to F1-ATPase. *Proc. Natl. Acad. Sci. U. S. A.* 111, 11305–11310. doi:10.1073/pnas.1411560111
- Bateman, A., Martin, M.-J., Orchard, S., Magrane, M., Agivetova, R., Ahmad, S., et al. (2021). UniProt: The universal protein knowledgebase in 2021. *Nucleic Acids Res.* 49, D480–D489. doi:10.1093/nar/gkaa1100
- Bhat, A. S., Dustin Schaeffer, R., Kinch, L., Medvedev, K. E., and Grishin, N. V. (2020). Recent advances suggest increased influence of selective pressure in allostery. *Curr. Opin. Struct. Biol.* 62, 183–188. doi:10.1016/j.sbi.2020.02.004
- Bosch, M. E., Bertrand, B. P., Heim, C. E., Alqarzaee, A. A., Chaudhari, S. S., Aldrich, A. L., et al. (2020). *Staphylococcus aureus* ATP synthase promotes biofilm persistence by influencing innate immunity. *MBio* 11, 015811–e1620. doi:10.1128/mBio.01581-20
- Bowler, M. W., Montgomery, M. G., Leslie, A. G. W., and Walker, J. E. (2007). Ground state structure of F1-ATPase from bovine heart mitochondria at 1.9 Å resolution. *J. Biol. Chem.* 282, 14238–14242. doi:10.1074/jbc.M700203200
- Cabezón, E., Montgomery, M. G., Leslie, A. G. W., and Walker, J. E. (2003). The structure of bovine F1-ATPase in complex with its regulatory protein IF1. *Nat. Struct. Biol.* 10, 744–750. doi:10.1038/nsb966
- Case, D., Betz, R., Cerutti, D., III, Cheatham, T. E., III, Darden, T. A., Duke, R. E., et al. (2016). *AMBER 16* San Francisco; University of California.
- Cataldi de Flombaum, M. A., and Stoppani, A. O. M. (1981). Influence of efrapeptin, aurovertin and citreoviridin on the mitochondrial adenosine triphosphatase from *Trypanosoma cruzi*. *Mol. Biochem. Parasitol.* 3, 143–155. doi:10.1016/0166-6851(81)90045-1
- Chang, C.-E., Chen, W., and Gilson, M. K. (2005). Evaluating the accuracy of the quasiharmonic approximation. *J. Chem. Theory Comput.* 1, 1017–1028. doi:10.1021/ct0500904
- Chang, T., and Penefsky, H. S. (1973). Aurovertin, a fluorescent probe of conformational change in beef heart mitochondrial adenosine triphosphatase. *J. Biol. Chem.* 248, 2746–2754. doi:10.1016/s0021-9258(19)44070-2
- Chatzigeorgoulas, A., and Courmia, Z. (2021). Rational design of allosteric modulators: Challenges and successes. *WIREs Comput. Mol. Sci.* 11, e1529. doi:10.1002/wcms.1529
- Cingolani, G., and Duncan, T. M. (2011). Structure of the ATP synthase catalytic complex (F1) from *Escherichia coli* in an autoinhibited conformation. *Nat. Struct. Mol. Biol.* 18, 701–707. doi:10.1038/nsmb.2058
- Cook, G. M., Hards, K., Vilchère, C., Hartman, T., and Berney, M. (2014). Energetics of respiration and oxidative phosphorylation in mycobacteria. *Microbiol. Spectr.* 2 (3), 1188–1190. doi:10.1128/microbiolspec.MGM2-0015-2013
- Crooks, G. E., Hon, G., Chandonia, J.-M., and Brenner, S. E. (2004). WebLogo: A sequence logo generator. *Genome Res.* 14, 1188–1190. doi:10.1101/gr.849004
- Darden, T., York, D., and Pedersen, L. (1993). Particle mesh Ewald: An $N \cdot \log(N)$ method for Ewald sums in large systems. *J. Chem. Phys.* 98, 10089–10092. doi:10.1063/1.464397
- Deuffhard, P., and Weber, M. (2005). Robust Perron cluster analysis in conformation dynamics. *Linear Algebra Appl.* 398, 161–184. doi:10.1016/j.laa.2004.10.026
- Duan, J., Li, Y., Gao, H., Yang, D., He, X., Fang, Y., et al. (2020). Phenolic compound ellagic acid inhibits mitochondrial respiration and tumor growth in lung cancer. *Food Funct.* 11, 6332–6339. doi:10.1039/d0fo01177k
- Eastman, P., Swails, J., Chodera, J. D., McGibbon, R. T., Zhao, Y., Beauchamp, K. A., et al. (2017). OpenMM 7: Rapid development of high performance algorithms for molecular dynamics. *PLOS Comput. Biol.* 13, e1005659. doi:10.1371/journal.pcbi.1005659
- Estabrook, R. A., Luo, J., Purdy, M. M., Sharma, V., Weakliem, P., Bruice, T. C., et al. (2005). Statistical coevolution analysis and molecular dynamics: Identification of amino acid pairs essential for catalysis. *Proc. Natl. Acad. Sci. U. S. A.* 102, 994–999. doi:10.1073/pnas.0409128102
- Fan, L., Wu, D., Goremykin, V., Xiao, J., Xu, Y., Garg, S., et al. (2020). Phylogenetic analyses with systematic taxon sampling show that mitochondria branch within Alphaproteobacteria. *Nat. Ecol. Evol.* 4, 1213–1219. doi:10.1038/s41559-020-1239-x
- Flores Francisco, B. G., Ponce, I. M., Plascencia Espinosa, M. Á., Mendieta Moctezuma, A., and López y López, V. E. (2021). Advances in the biological control of phytoparasitic nematodes via the use of nematophagous fungi. *World J. Microbiol. Biotechnol.* 37, 180. doi:10.1007/s11274-021-03151-x
- Franco-Serrano, L., Huerta, M., Hernández, S., Cedano, J., Perez-Pons, J. A., Piñol, J., et al. (2018). Multifunctional proteins: Involvement in human diseases and targets of current drugs. *Protein J.* 37, 444–453. doi:10.1007/s10930-018-9790-x
- Galber, C., Carissimi, S., Baracca, A., and Giorgio, V. (2021). The ATP synthase deficiency in human diseases. *Life* 11, 325. doi:10.3390/life11040325
- García-Hernández, E., Hernández-Arana, A., and Hernandez-ArAnA, A. (1999). Structural bases of lectin-carbohydrate affinities: Comparison with protein-folding energetics. *Protein Sci.* 8, 1075–1086. doi:10.1110/ps.8.5.1075
- Genheden, S., and Ryde, U. (2015). The MM/PBSA and MM/GBSA methods to estimate ligand-binding affinities. *Expert Opin. Drug Discov.* 10, 449–461. doi:10.1517/17460441.2015.1032936
- Gledhill, J. R., Montgomery, M. G., Leslie, A. G. W., and Walker, J. E. (2007b). How the regulatory protein, IF1, inhibits F1-ATPase from bovine mitochondria. *Proc. Natl. Acad. Sci. U. S. A.* 104, 15671–15676. doi:10.1073/pnas.0707326104
- Gledhill, J. R., Montgomery, M. G., Leslie, A. G. W., and Walker, J. E. (2007a). Mechanism of inhibition of bovine F1-ATPase by resveratrol and related polyphenols. *Proc. Natl. Acad. Sci. U. S. A.* 104, 13632–13637. doi:10.1073/pnas.0706290104
- Groth, G., and Pohl, E. (2001). The structure of the chloroplast F1-ATPase at 3.2 Å resolution. *J. Biol. Chem.* 276, 1345–1352. doi:10.1074/jbc.M008015200
- Gu, J., Zhang, L., Zong, S., Guo, R., Liu, T., Yi, J., et al. (2019). Cryo-EM structure of the mammalian ATP synthase tetramer bound with inhibitory protein IF1. *Science* 364, 1068–1075. doi:10.1126/science.aaw4852
- Guo, H., Courbon, G. M., Bueler, S. A., Mai, J., Liu, J., and Rubinstein, J. L. (2021). Structure of mycobacterial ATP synthase bound to the tuberculosis drug bedaquiline. *Nature* 589, 143–147. doi:10.1038/s41586-020-3004-3
- Hards, K., and Cook, G. M. (2018). Targeting bacterial energetics to produce new antimicrobials. *Drug resist. updat.* 36, 1–12. doi:10.1016/j.drup.2017.11.001
- Hicks, D. B., and Krulwich, T. A. (1995). The respiratory chain of alkaliphilic bacteria. *Biochim. Biophys. Acta* 1229, 303–314. doi:10.1016/0005-2728(95)00024-D
- Hoffman, P. S. (2020). Antibacterial discovery: 21st century challenges. *Antibiotics* 9, 213. doi:10.3390/antibiotics9050213
- Hong, S., and Pedersen, P. L. (2008). ATP synthase and the actions of inhibitors utilized to study its roles in human health, disease, and other scientific areas. *Microbiol. Mol. Biol. Rev.* 72, 590–641. doi:10.1128/mmbr.00016-08
- Hong, S., and Pedersen, P. L. (2003). ATP synthases: Insights into their motor functions from sequence and structural analyses. *J. Bioenerg. Biomembr.* 35, 95–120. doi:10.1023/a:1023786618422

- Hopkins, C. W., Le Grand, S., Walker, R. C., and Roitberg, A. E. (2015). Long-time-step molecular dynamics through hydrogen mass repartitioning. *J. Chem. Theory Comput.* 11, 1864–1874. doi:10.1021/ct5010406
- Huang, T.-C., Chang, H.-Y., Hsu, C.-H., Kuo, W.-H., Chang, K.-J., and Juan, H.-F. (2008). Targeting therapy for breast carcinoma by ATP synthase inhibitor aurovertin B. *J. Proteome Res.* 7, 1433–1444. doi:10.1021/pr700742h
- Husic, B. E., and Pande, V. S. (2018). Markov state models: From an art to a science. *J. Am. Chem. Soc.* 140, 2386–2396. doi:10.1021/jacs.7b12191
- Ichikawa, N., Chisuwa, N., Tanase, M., and Nakamura, M. (2005). Mitochondrial ATP synthase residue betaarginine-408, which interacts with the inhibitory site of regulatory protein IF1, is essential for the function of the enzyme. *J. Biochem.* 138, 201–207. doi:10.1093/jb/mvi116
- Ichiye, T., and Karplus, M. (1991). Collective motions in proteins: A covariance analysis of atomic fluctuations in molecular dynamics and normal mode simulations. *Proteins* 11, 205–217. doi:10.1002/prot.340110305
- Issartel, J. P., Klein, G., Satre, M., and Vignais, P. V. (1983a). Aurovertin binding sites on beef heart mitochondrial F1-ATPase. Study with [¹⁴C]aurovertin D of the binding stoichiometry and of the interaction between aurovertin and the natural ATPase inhibitor for binding to F1. *Biochemistry* 22, 3492–3497. doi:10.1021/bi00283a028
- Issartel, J. P., Klein, G., Satre, M., and Vignais, P. V. (1983b). Binding of [¹⁴C]aurovertin D to *Escherichia coli* F1-ATPase and the isolated .beta. subunit. Correlation with inhibition of the ATPase activity. *Biochemistry* 22, 3485–3492. doi:10.1021/bi00283a027
- Issartel, J. P., and Vignais, P. V. (1984). Evidence for a nucleotide binding site on the isolated β subunit from *Escherichia coli* F1-ATPase. Interaction between nucleotide and aurovertin D binding sites. *Biochemistry* 23, 6591–6595. doi:10.1021/bi00321a048
- Jarman, O. D., Biner, O., and Hirst, J. (2021). Regulation of ATP hydrolysis by the ϵ subunit, ζ subunit and Mg-ADP in the ATP synthase of *Paracoccus denitrificans*. *Biochim. Biophys. Acta. Bioenerg.* 1862, 148355. doi:10.1016/j.bbabi.2020.148355
- Johnson, K. M., Swenson, L., Opiari, A. W., Reuter, R., Zarrabi, N., Fierke, C. A., et al. (2009). Mechanistic basis for differential inhibition of the F1Fo-ATPase by aurovertin. *Biopolymers* 91, 830–840. doi:10.1002/bip.21262
- Jorgensen, W. L., Chandrasekhar, J., Madura, J. D., Impey, R. W., and Klein, M. L. (1983). Comparison of simple potential functions for simulating liquid water. *J. Chem. Phys.* 79, 926–935. doi:10.1063/1.445869
- Kühlbrandt, W. (2019). Structure and mechanisms of F-type ATP synthases. *Annu. Rev. Biochem.* 88, 515–549. doi:10.1146/annurev-biochem-013118-110903
- Lakshmanan, M., and Xavier, A. S. (2013). Bedaquiline - the first ATP synthase inhibitor against multi drug resistant tuberculosis. *J. Young Pharm.* 5, 112–115. doi:10.1016/j.jyp.2013.12.002
- Lee, R. S. F., Pagan, J., Satre, M., Vignais, P. V., and Senior, A. E. (1989). Identification of a mutation in *Escherichia coli* F1-ATPase β -subunit conferring resistance to aurovertin. *FEBS Lett.* 253, 269–272. doi:10.1016/0014-5793(89)80973-1
- Lee, R. S. F., Pagan, J., Wilke-Mounts, S., and Senior, A. E. (1991). Characterization of *Escherichia coli* ATP synthase β -subunit mutations using a chromosomal deletion strain. *Biochemistry* 30, 6842–6847. doi:10.1021/bi00242a006
- Leipe, D. D., Koonin, E. V., and Aravind, L. (2003). Evolution and classification of P-loop kinases and related proteins. *J. Mol. Biol.* 333, 781–815. doi:10.1016/j.jmb.2003.08.040
- Livingstone, C. D., and Barton, G. J. (1993). Protein sequence alignments: A strategy for the hierarchical analysis of residue conservation. *Comput. Appl. Biosci.* 9, 745–756. doi:10.1093/bioinformatics/9.6.745
- Lu, S., Shen, Q., and Zhang, J. (2019). Allosteric methods and their applications: Facilitating the discovery of allosteric drugs and the investigation of allosteric mechanisms. *Acc. Chem. Res.* 52, 492–500. doi:10.1021/acs.accounts.8b00570
- Luo, M., Zhou, W., Patel, H., Srivastava, A. P., Symersky, J., Bonar, M. M., et al. (2020). Bedaquiline inhibits the yeast and human mitochondrial ATP synthases. *Commun. Biol.* 3, 452. doi:10.1038/s42003-020-01173-z
- Mahajan, R. (2013). Bedaquiline: First FDA-approved tuberculosis drug in 40 years. *Int. J. Appl. Basic Med. Res.* 3, 1–2. doi:10.4103/2229-516X.112228
- Maier, J. A., Martinez, C., Kasavajhala, K., Wickstrom, L., Hauser, K. E., and Simmerling, C. (2015). ff14SB: Improving the accuracy of protein side chain and backbone parameters from ff99SB. *J. Chem. Theory Comput.* 11, 3696–3713. doi:10.1021/acs.jctc.5b00255
- Mao, H. Z., Abraham, C. G., Krishnakumar, A. M., and Weber, J. (2008). A functionally important hydrogen-bonding network at the betaDP/alphaDP interface of ATP synthase. *J. Biol. Chem.* 283, 24781–24788. doi:10.1074/jbc.M804142200
- Meagher, K. L., Redman, L. T., and Carlson, H. A. (2003). Development of polyphosphate parameters for use with the AMBER force field. *J. Comput. Chem.* 24, 1016–1025. doi:10.1002/jcc.10262
- Miller, B. R., McGee, T. D., Swails, J. M., Homeyer, N., Gohlke, H., and Roitberg, A. E. (2012). MMPBSA.py: An efficient program for end-state free energy calculations. *J. Chem. Theory Comput.* 8, 3314–3321. doi:10.1021/ct300418h
- Miyamoto, S., and Kollman, P. A. (1992). Settle: An analytical version of the SHAKE and RATTLE algorithm for rigid water models. *J. Comput. Chem.* 13, 952–962. doi:10.1002/jcc.540130805
- Morales-Rios, E., Montgomery, M. G., Leslie, A. G. W., and Walker, J. E. (2015). Structure of ATP synthase from *Paracoccus denitrificans* determined by X-ray crystallography at 4.0 Å resolution. *Proc. Natl. Acad. Sci. U. S. A.* 112, 13231–13236. doi:10.1073/pnas.1517542112
- Nesci, S., Trombetti, F., Algieri, C., and Pagliarini, A. (2019). A therapeutic role for the F1Fo-ATP synthase. *SLAS Discov.* 24, 893–903. doi:10.1177/2472555219860448
- Nussinov, R., and Tsai, C.-J. (2012). The different ways through which specificity works in orthosteric and allosteric drugs. *Curr. Pharm. Des.* 18, 1311–1316. doi:10.2174/138161212799436377
- O'Boyle, N. M., Banck, M., James, C. A., Morley, C., Vandermeersch, T., and Hutchison, G. R. (2011). Open Babel: An open chemical toolbox. *J. Cheminform.* 3, 33. doi:10.1186/1758-2946-3-33
- Pande, V. S., Beauchamp, K., and Bowman, G. R. (2010). Everything you wanted to know about Markov State Models but were afraid to ask. *Methods* 52, 99–105. doi:10.1016/j.ymeth.2010.06.002
- Patel, B. A., D'Amico, T. L., and Blagg, B. S. J. (2020). Natural products and other inhibitors of F1Fo ATP synthase. *Eur. J. Med. Chem.* 207, 112779. doi:10.1016/j.ejmech.2020.112779
- Pettersen, E. F., Goddard, T. D., Huang, C. C., Couch, G. S., Greenblatt, D. M., Meng, E. C., et al. (2004). UCSF Chimera - a visualization system for exploratory research and analysis. *J. Comput. Chem.* 25, 1605–1612. doi:10.1002/jcc.20084
- Pettersen, E. F., Goddard, T. D., Huang, C. C., Meng, E. C., Couch, G. S., Croll, T. I., et al. (2021). UCSF ChimeraX: Structure visualization for researchers, educators, and developers. *Protein Sci.* 30, 70–82. doi:10.1002/pro.3943
- Pulido, N. O., Salcedo, G., Pérez-Hernández, G., José-Núñez, C., Velázquez-Campoy, A., and García-Hernández, E. (2010). Energetic effects of magnesium in the recognition of adenosine nucleotides by the F1-ATPase β subunit. *Biochemistry* 49, 5258–5268. doi:10.1021/bi1006767
- Rachman, M., Bajusz, D., Hetényi, A., Scarpino, A., Meró, B., Egyed, A., et al. (2020). Discovery of a novel kinase hinge binder fragment by dynamic undocking. *RSC Med. Chem.* 11, 552–558. doi:10.1039/C9MD00519F
- Raza, S., Ranaghan, K. E., van der Kamp, M. W., Woods, C. J., Mulholland, A. J., and Azam, S. S. (2019). Visualizing protein–ligand binding with chemical energy-wise decomposition (CHEWD): Application to ligand binding in the kallikrein-8 S1 site. *J. Comput. Aided. Mol. Des.* 33, 461–475. doi:10.1007/s10822-019-00200-4
- Reisman, B. J., Guo, H., Ramsey, H. E., Wright, M. T., Reinfield, B. I., Ferrell, P. B., et al. (2022). Apoptolidin family glycomacrolides target leukemia through inhibition of ATP synthase. *Nat. Chem. Biol.* 18, 360–367. doi:10.1038/s41589-021-00900-9
- Roe, D. R., and Cheatham, T. E. (2013). PTRAJ and CPPTRAJ: Software for processing and analysis of molecular dynamics trajectory data. *J. Chem. Theory Comput.* 9, 3084–3095. doi:10.1021/ct400341p
- Roger, A. J., Muñoz-Gómez, S. A., and Kamikawa, R. (2017). The origin and diversification of mitochondria. *Curr. Biol.* 27, R1177–R1192. doi:10.1016/j.cub.2017.09.015
- Ruiz-Blanco, Y. B., Ávila-Barrientos, L. P., Hernández-García, E., Antunes, A., Agüero-Chapin, G., and García-Hernández, E. (2021). Engineering protein fragments via evolutionary and protein–protein interaction algorithms: De novo design of peptide inhibitors for FOF1-ATP synthase. *FEBS Lett.* 595, 183–194. doi:10.1002/1873-3468.13988
- Ruiz-Carmona, S., Alvarez-Garcia, D., Foloppe, N., Garmendia-Doval, A. B., Juhos, S., Schmidtke, P., et al. (2014). rDock: A fast, versatile and open source program for docking ligands to proteins and nucleic acids. *PLoS Comput. Biol.* 10, e1003571. doi:10.1371/journal.pcbi.1003571
- Ryckaert, J. P., Ciccotti, G., and Berendsen, H. J. C. (1977). Numerical integration of the cartesian equations of motion of a system with constraints: Molecular dynamics of n-alkanes. *J. Comput. Phys.* 23, 327–341. doi:10.1016/0021-9991(77)90098-5
- Saishu, T., Kagawa, Y., and Shimizu, R. (1983). Resistance of thermophilic atpase (TF1) to specific F1-atpase inhibitors including local anesthetics. *Biochem. Biophys. Res. Commun.* 112, 822–826. doi:10.1016/0006-291X(83)91691-1

- Salcedo, G., Cano-Sánchez, P., De Gómez-Puyou, M. T., Velázquez-Campoy, A., and García-Hernández, E. (2014). Isolated noncatalytic and catalytic subunits of F1-ATPase exhibit similar, albeit not identical, energetic strategies for recognizing adenosine nucleotides. *Biochim. Biophys. Acta* 1837, 44–50. doi:10.1016/j.bbabi.2013.08.005
- Šali, A., Blundell, T. L., and Sali, A. (1993). Comparative protein modelling by satisfaction of spatial restraints. *J. Mol. Biol.* 234, 779–815. doi:10.1006/jmbi.1993.1626
- Salomon-Ferrer, R., Götz, A. W., Poole, D., Le Grand, S., and Walker, R. C. (2013). Routine microsecond molecular dynamics simulations with AMBER on GPUs. 2. Explicit solvent particle mesh Ewald. *J. Chem. Theory Comput.* 9, 3878–3888. doi:10.1021/ct400314y
- Satre, M., Klein, G., and Vignais, P. V. (1979). Isolation of aurovertin-resistant mutants from *Escherichia coli*. *Methods Enzymol.* 56, 178–182. doi:10.1016/0076-6879(79)56020-0
- Scherer, M. K., Trendelkamp-Schroer, B., Paul, F., Pérez-Hernández, G., Hoffmann, M., Plattner, N., et al. (2015). PyEMMA 2: A software package for estimation, validation, and analysis of Markov models. *J. Chem. Theory Comput.* 11, 5525–5542. doi:10.1021/acs.jctc.5b00743
- Sekiya, M., Sakamoto, Y., Futai, M., and Nakanishi-Matsui, M. (2017). Role of α/β interface in F1 ATPase rotational catalysis probed by inhibitors and mutations. *Int. J. Biol. Macromol.* 99, 615–621. doi:10.1016/j.ijbiomac.2017.02.089
- Shapovalov, M. V., and Dunbrack, R. L. (2011). A smoothed backbone-dependent rotamer library for proteins derived from adaptive kernel density estimates and regressions. *Structure* 19, 844–858. doi:10.1016/j.str.2011.03.019
- Sheik Amamuddy, O., Veldman, W., Manyumwa, C., Khairallah, A., Agajanian, S., Oluyemi, O., et al. (2020). Integrated computational approaches and tools for allosteric drug discovery. *Int. J. Mol. Sci.* 21, 847. doi:10.3390/ijms21030847
- Sievers, F., Wilm, A., Dineen, D., Gibson, T. J., Karplus, K., Li, W., et al. (2011). Fast, scalable generation of high-quality protein multiple sequence alignments using Clustal Omega. *Mol. Syst. Biol.* 7, 539. doi:10.1038/msb.2011.75
- Sobti, M., Ueno, H., Noji, H., and Stewart, A. G. (2021). The six steps of the complete F1-ATPase rotary catalytic cycle. *Nat. Commun.* 12, 4690. doi:10.1038/s41467-021-25029-0
- Sobti, M., Walshe, J. L., Wu, D., Ishmukhametov, R., Zeng, Y. C., Robinson, C. V., et al. (2020). Cryo-EM structures provide insight into how *E. coli* F1Fo ATP synthase accommodates symmetry mismatch. *Nat. Commun.* 11, 2615. doi:10.1038/s41467-020-16387-2
- Srivastava, A. P., Luo, M., Zhou, W., Symersky, J., Bai, D., Chambers, M. G., et al. (2018). High-resolution cryo-EM analysis of the yeast ATP synthase in a lipid membrane. *Sci. (80-)* 360, eaas9699. doi:10.1126/science.aas9699
- Stein, S. A. M., Loccisano, A. E., Firestine, S. M., and Evanseck, J. D. (2006). Chapter 13 principal components analysis: A review of its application on molecular dynamics data. *Annu. Rep. Comput. Chem.* 2, 233–261. doi:10.1016/S1574-1400(06)02013-5
- Symersky, J., Osowski, D., Walters, D. E., and Mueller, D. M. (2012). Oligomycin frames a common drug-binding site in the ATP synthase. *Proc. Natl. Acad. Sci. U. S. A.* 109, 13961–13965. doi:10.1073/pnas.1207912109
- Talibov, V. O., Fabini, E., FitzGerald, E. A., Tedesco, D., Cederfeldt, D., Talu, M. J., et al. (2021). Discovery of an allosteric ligand binding site in SMYD3 lysine methyltransferase. *ChemBiochem.* 22, 1597–1608. doi:10.1002/cbic.202000736
- Tan, C., Tan, Y.-H., and Luo, R. (2007). Implicit nonpolar solvent models. *J. Phys. Chem. B* 111, 12263–12274. doi:10.1021/jp073399n
- Tan, C., Yang, L., and Luo, R. (2006). How well does Poisson–Boltzmann implicit solvent agree with explicit solvent? A quantitative analysis. *J. Phys. Chem. B* 110, 18680–18687. doi:10.1021/jp063479b
- Taurino, F., and Gnoni, A. (2018). Systematic review of plasma-membrane ecto-ATP synthase: A new player in health and disease. *Exp. Mol. Pathol.* 104, 59–70. doi:10.1016/j.yexmp.2017.12.006
- van Raaij, M. J., Abrahams, J. P., Leslie, A. G. W. W., and Walker, J. E. (1996). The structure of bovine F1-ATPase complexed with the antibiotic inhibitor aurovertin B. *Proc. Natl. Acad. Sci. U. S. A.* 93, 6913–6917. doi:10.1073/pnas.93.14.6913
- Varghese, F., Blaza, J. N., Jones, A. J. Y., Jarman, O. D., and Hirst, J. (2018). Deleting the IF1-like ζ subunit from *Paracoccus denitrificans* ATP synthase is not sufficient to activate ATP hydrolysis. *Open Biol.* 8, 170206. doi:10.1098/rsob.170206
- Vasan, N., Baselga, J., and Hyman, D. M. (2019). A view on drug resistance in cancer. *Nature* 575, 299–309. doi:10.1038/s41586-019-1730-1
- Verschuur, G. J., van der Sluis, P. R., and Slater, E. C. (1977). The binding of aurovertin to isolated β subunit of F1 (mitochondrial ATPase) stoichiometry of β subunit in F1. *Biochim. Biophys. Acta* 462, 438–449. doi:10.1016/0005-2728(77)90141-4
- Vestergaard, M., Roshanak, S., and Ingmer, H. (2021). Targeting the ATP synthase in *Staphylococcus aureus* small colony Variants *Streptococcus pyogenes* and pathogenic fungi. *Antibiot. (Basel, Switz.,)* 10, 376. doi:10.3390/antibiotics10040376
- Walker, J. E., Saraste, M., Runswick, M. J., and Gay, N. J. (1982). Distantly related sequences in the alpha- and beta-subunits of ATP synthase, myosin, kinases and other ATP-requiring enzymes and a common nucleotide binding fold. *EMBO J.* 1, 945–951. doi:10.1002/j.1460-2075.1982.tb01276.x
- Wang, C., Greene, D., Xiao, L., Qi, R., and Luo, R. (2018). Recent developments and applications of the MMPBSA method. *Front. Mol. Biosci.* 4, 87. doi:10.3389/fmolb.2017.00087
- Wang, E., Sun, H., Wang, J., Wang, Z., Liu, H., Zhang, J. Z. H., et al. (2019). End-point binding free energy calculation with MM/PBSA and MM/GBSA: Strategies and applications in drug design. *Chem. Rev.* 119, 9478–9508. doi:10.1021/acs.chemrev.9b00055
- Wang, J., Wolf, R. M., Caldwell, J. W., Kollman, P. A., and Case, D. A. (2004). Development and testing of a general Amber force field. *J. Comput. Chem.* 25, 1157–1174. doi:10.1002/jcc.20035
- Wang, T., Ma, F., and Qian, H. L. (2021). Defueling the cancer: ATP synthase as an emerging target in cancer therapy. *Mol. Ther. Oncolytics* 23, 82–95. doi:10.1016/j.omto.2021.08.015
- Waterhouse, A. M., Procter, J. B., Martin, D. M. A., Clamp, M., and Barton, G. J. (2009). Jalview Version 2—a multiple sequence alignment editor and analysis workbench. *Bioinformatics* 25, 1189–1191. doi:10.1093/bioinformatics/btp033
- Wu, R., Yang, X., Zhou, Q., Yu, W., Li, M., Wo, J., et al. (2020). Aurovertin B exerts potent antitumor activity against triple-negative breast cancer *in vivo* and *in vitro* via regulating ATP synthase activity and DUSP1 expression. *Pharmazie* 75, 261–265. doi:10.1691/ph.2020.0380
- Ye, X., Wang, J., and Luo, R. (2010). A revised density function for molecular surface definition in continuum solvent models. *J. Chem. Theory Comput.* 6, 1157–1169. doi:10.1021/ct900318u
- Zhang, A. T., Montgomery, M. G., Leslie, A. G. W., Cook, G. M., and Walker, J. E. (2019). The structure of the catalytic domain of the ATP synthase from *Mycobacterium smegmatis* is a target for developing antitubercular drugs. *Proc. Natl. Acad. Sci. U. S. A.* 116, 4206–4211. doi:10.1073/pnas.1817615116